

Optimally band-limited controls for quantum multi-axis spectral estimation

Virginia Frey,¹ Leigh M. Norris,² Lorenza Viola,² and Michael J. Biercuk^{1,*}

¹*ARC Centre for Engineered Quantum Systems, School of Physics, The University of Sydney, NSW 2006 Australia*

²*Department of Physics and Astronomy, Dartmouth College, 6127 Wilder Laboratory, Hanover, NH 03755, USA*

(Dated: November 7, 2019)

The fragility of quantum systems makes them ideally suited for sensing applications at the nanoscale. However, interpreting the output signal of a qubit-based sensor is generally complicated by background clutter due to out-of-band spectral leakage, as well as ambiguity in signal origin when the sensor is operated with imperfect hardware. Here, we present a sensing protocol based on optimally band-limited “Slepian functions” that can overcome these challenges, by providing narrowband sensing of ambient dephasing noise, coupling additively to the sensor along the z -axis, while permitting isolation of the target noise spectrum from other contributions coupling along a different axis. This is achieved by introducing a new finite-difference control modulation, which linearizes the sensor’s response and affords tunable band-limited “windowing” of the sensor in frequency. Building on these techniques, we experimentally demonstrate two new spectral estimation capabilities using a trapped-ion qubit sensor. We first perform efficient experimental reconstruction of a “mixed” dephasing spectrum, composed of a broadband $1/f$ -type spectrum with discrete spurs. We then demonstrate the simultaneous reconstruction of overlapping dephasing and control noise spectra from a single set of measurements, in a setting where the two spectra contribute equally to the sensor’s response. Our approach provides a direct means to augment quantum-sensor performance in the presence of both complex broadband noise environments and imperfect control signals, by optimally complying with realistic time-bandwidth constraints.

Quantum sensors harness a feature which is otherwise regarded as the central weakness of quantum technologies as a resource: their extreme sensitivity to external disturbances. Applications range from magnetometry and medical imaging to noise characterization for optimized control design in intermediate-scale quantum computers and simulators [1–3]. In conventional operation, and in the simplest setting where a single qubit is employed as a sensor, the sensor undergoes a simple evolution during which an integrated signal from the environment changes the qubit’s state in a measurable way [1]. This form of “Ramsey experiment” exhibits broad-band coupling to the environment with sensitivity down to DC.

Adding time-dependent control to the sensor provides a means to adjust its spectral response – as is needed for applications in frequency-tuned sensing [4–6]. This general approach has been employed in dynamical-decoupling noise spectroscopy protocols in either pulsed [2, 3, 7] or continuously-driven form [8], as well as in spin-locking-based protocols [9, 10]. However, existing spectral estimation approaches leveraging such protocols suffer from significant drawbacks. First, while pulsed protocols have been recently extended to estimation of general multi-axis additive noise in principle [11], they involve abrupt transitions in the amplitude or phase of the applied control [12–16], which inevitably result in additional sensitivity outside of the target frequency band. This phenomenon, known as *spectral leakage*, can cause ambiguity in the interpretation of the sensor response, as out-of-band signals can couple to harmonics of the target band induced by the rapid control transitions [17, 18]. Second, any imperfections on the control itself, or contributions from other unwanted Hamiltonian terms, are manifested as deviations in the qubit-sensor’s state that are indistinguishable from the target signal in conventional projective measurements.

Here, we present a continuously driven, smoothly modulated control protocol for qubit sensors, which employs optimally band-limited Slepian functions, more formally known as *discrete prolate spheroidal sequences* (DPSS) [19]. Widely

used in classical statistical signal processing [20], DPSS have recently found application in optimal control algorithms for quantum gate synthesis [21] and enabled a proof-of-concept demonstration of multitaper spectral estimation in the limited setting of noise along a single axis – colinear (hence commuting) with the applied control [22, 23]. Extending the approach to non-commuting additive dephasing noise ($\propto \sigma_z$), while maintaining the desired spectral concentration in the frequency domain, requires introducing a qualitatively different control modulation, able to linearize the sensor’s response and effectively invert the ensuing non-linearity via a finite-difference scheme. We show that this approach, coupled with tomographic measurement of the sensor’s state, provides simultaneous, tunable, narrowband responses to *both* the non-commuting dephasing signal and commuting, multiplicative noise terms as may arise from the control hardware. We experimentally demonstrate the efficacy of these controls using a single trapped $^{171}\text{Yb}^+$ ion, by mapping the filter function [24–27] of the control in multiple Cartesian projections. We then demonstrate the ability to reconstruct an engineered mixed dephasing spectrum, composed of both broadband and narrowband features, through a Bayesian estimation procedure. Finally, we leverage the narrowband properties of our controls along multiple Cartesian projections to simultaneously reconstruct two overlapping spectra, arising from noise in the amplitude ($\propto \sigma_x$) and phase ($\propto \sigma_z$) quadratures, using the *same* set of tomographic measurements.

Results

System and control setting. In previous work [22, 23], we showed how qubit-sensors controlled with DPSS-shaped waveforms possess a narrowband frequency response for a target noise coupling via a Hamiltonian term which commutes with the applied control, exhibiting provably optimal out-of-band rejection. We now move beyond this limited setting and include non-commutative dephasing processes. In this case, as is common in various quantum-sensing settings including magnetometry [1], the target signal is manifested as an addi-

arXiv:1911.02005v1 [quant-ph] 1 Nov 2019
essentially, the control resulting in the sensor responding to effects from other freq bands

why?

tive “dephasing” term in the Hamiltonian $\propto \sigma_z$.

To formulate the estimation problem of interest, it is convenient to describe the controlled qubit dynamics in the presence of noise in a frame which co-rotates with the carrier frequency and at resonance with the qubit transition. Assuming that the ideal control corresponds to time-dependent amplitude modulation via a Hamiltonian of the form $H_{\text{ctrl}}(t) \equiv \Omega(t)\sigma_x/2$, the total Hamiltonian reads [23, 25] ($\hbar = 1$):

$$H(t) = \beta_z(t)\sigma_z + \Omega(t)[1 + \beta_\Omega(t)]\sigma_x/2. \quad (1)$$

Here, $\Omega(t)$ is the amplitude of the driving field, which is tunable within a maximum range $|\Omega| \leq \Omega_{\max}$, and $\beta_z, \beta_\Omega(t)$ are stochastic processes modeling time-dependent noise in the target dephasing and control quadratures, respectively. We treat these two processes as independent, with each being stationary, Gaussian, and zero-mean. The noise properties are then fully characterized in terms of the power spectral densities, obtained through the Fourier transforms of the auto-correlation functions: $S_u(\omega) = \frac{1}{2\pi} \int_{-\infty}^{\infty} ds \langle \beta_u(0)\beta_u(s) \rangle e^{-is\omega}$, for $u \in \{\Omega, z\}$.

By effecting an additional transformation to a frame that co-rotates with the ideal control, the Hamiltonian (1) maps to

$$\tilde{H}(t) = [\cos \Theta(t)\sigma_z + \sin \Theta(t)\sigma_y]\beta_z(t) + \Omega(t)\beta_\Omega(t)\sigma_x/2,$$

where the integrated angle of driven rotation is $\Theta(t) \equiv \int_0^t ds \Omega(s)$. In this frame, time evolution is described by the unitary propagator $\tilde{U}(t) = \mathcal{T}_+ \exp \left[\int_0^t ds \tilde{H}(s) \right] \equiv \exp[-ia(t) \cdot \boldsymbol{\sigma}]$, where $\boldsymbol{\sigma}$ is the Pauli vector and we have defined $\mathbf{a}(t) \equiv [a_x(t), a_y(t), a_z(t)]$ as a real, time-dependent “error vector” [25]. We have chosen a Cartesian representation, as it maps to standard tomographic protocols for measuring qubit state projections. Throughout our analysis and experiments, we shall work in a regime where the noise is sufficiently weak and the time scales are sufficiently small, such that we only need to consider the leading (first) order terms in a perturbative Magnus expansion of the error vector [16, 23, 28], that is, $\mathbf{a}(t) \approx \mathbf{a}^{(1)}(t)$. Explicitly, we have:

$$a_x^{(1)}(t) = \frac{1}{2} \int_0^t ds \Omega(s)\beta_\Omega(s), \quad (2a)$$

$$a_y^{(1)}(t) = \int_0^t ds \sin \Theta(s)\beta_z(s), \quad (2b)$$

$$a_z^{(1)}(t) = \int_0^t ds \cos \Theta(s)\beta_z(s). \quad (2c)$$

Here the control noise, $\beta_\Omega(t)$, enters $a_x^{(1)}$ in a way that is linearly proportional to the control variable, $\Omega(t)$; in contrast, in both the $a_y^{(1)}$ and $a_z^{(1)}$ components, the dephasing signal, $\beta_z(t)$, couples to $\Omega(t)$ through a nonlinear function of $\Theta(t)$.

Moving to the frequency domain, the action of the external control is most conveniently described within the filter function (FF) formalism [25, 27–29]. By using the explicit form of $H_{\text{ctrl}}(t)$, three fundamental FFs suffice to evaluate how the

sensor’s response to dephasing and amplitude noise is modified by the control [23], namely, the Fourier transforms

$$F_{xx}(\omega, t) \equiv \int_0^t ds \Omega(s)e^{i\omega s}, \quad (3a)$$

$$F_{zy}(\omega, t) \equiv \int_0^t ds \sin \Theta(s)e^{i\omega s}, \quad (3b)$$

with a similar expression defining $F_{zz}(\omega, t)$ (see also Supplementary Note 1). The error vector components from Eq. (2) may then be expressed as overlap integrals between appropriate FFs and the corresponding noise spectra,

$$\langle |a_x^{(1)}(t)|^2 \rangle = \frac{1}{\pi} \int_0^\infty d\omega F_\Omega(\omega, t) S_\Omega(\omega), \quad (4a)$$

$$\langle |a_y^{(1)}(t)|^2 \rangle = \frac{1}{\pi} \int_0^\infty d\omega F_z(\omega, t) S_z(\omega), \quad (4b)$$

where $\langle \cdot, \cdot \rangle$ denotes ensemble averages taken over all possible time-domain realisations of the stochastic process, and the *amplitude FF* and *dephasing FF* are, respectively, given by $F_\Omega(\omega, t) \equiv \frac{1}{4}|F_{xx}(\omega, t)|^2$ and $F_z(\omega, t) \equiv |F_{zy}(\omega, t)|^2$.

The primary tool available for shaping these filters and thus changing the sensor’s spectral response is temporal modulation of the control amplitude, $\Omega(t)$. Common control protocols like, for instance, Carr-Purcell-Meiboom-Gill (CPMG) sequences are known to provide a tunable response of the sensor to the target spectrum (see Fig. 1b). In the limit of instantaneous π_x pulses, the control-dependent term in Eq. (2c) becomes a piecewise-constant function $y(t)$ that switches between ± 1 whenever a pulse is applied. The corresponding FF, given by the Fourier transform of this rectangular switching function, has then a sinc-like shape with infinite harmonics at integer multiples of the pulse separation.

Continuous modulation of $\Omega(t)$ can be employed to reduce spectral leakage associated with such sharp transitions, however care must be taken to deal with the highly nonlinear way in which $a_y^{(1)}(t)$ (or $a_z^{(1)}(t)$) depend upon $\Omega(t)$. Because of this, the dephasing FF under DPSS control is generally *not* spectrally concentrated and thus not suited for “nonparametric” estimation [20], where no *a priori* knowledge about the target signal is assumed. This stands in contrast to the amplitude FF, which exhibits narrowband response under DPSS control thanks to the linearity on $\Omega(t)$ in Eq. (2a) [22, 23]. Nonlinearity breaks not only the spectral concentration, but also the ability to spectrally tune the sensor when driven with continuous modulation. This is illustrated in Fig. 1c: comparing the dephasing FFs of CPMG vs. DPSS controls reveals a breakdown in the peaked sensor response for the latter, irrespective of residual spectral leakage for pulsed control.

Spectral concentration via finite-difference control. To overcome this fundamental limitation, we return to an analysis of the sensor’s noise admittance under these controls. The challenge is to devise a smoothly varying time-domain control modulation $\Omega(t)$, which guarantees a spectrally concen-

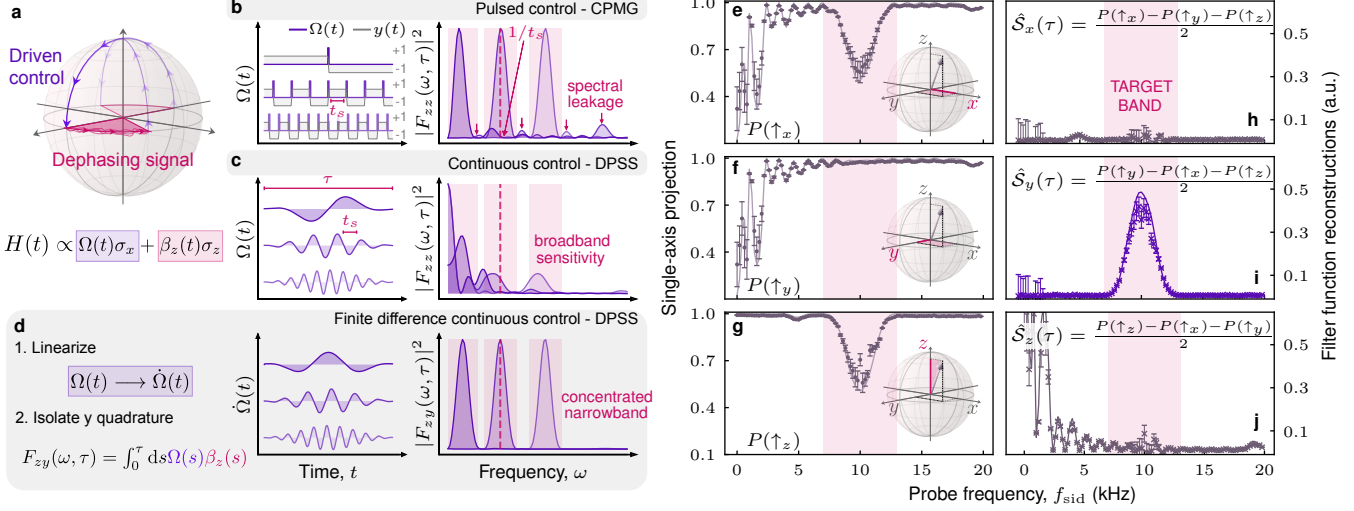


FIG. 1. Designing spectrally concentrated filters for dephasing sensing. **a** illustrates the dephasing sensing process (Hamiltonian in Eq. (1) with $\beta_\Omega(t) \equiv 0$), involving periods of phase accumulation under the dephasing process $\beta_z(t)$ and driven control $\Omega(t)$. **b, c** show $\Omega(t)$ for conventional sensing sequences and the corresponding FFs for both pulsed (CPMG) and continuous (DPSS) modulation. The FF for pulsed control, $|F_{zz}(\omega, \tau)|^2 = |\int_0^\tau ds e^{i\omega s} y(s)|^2$, exhibits harmonics at $\omega = \pi n/t_s$ for integer $n \geq 1$. For the DPSS modulation in **c**, $F_z(\omega, \tau) = |F_{xy}(\omega, \tau)|^2$ is broadband sensitive. **d** Finite-difference controls linearize the sensor response to the target dephasing signal. The corresponding FFs are tunable and spectrally concentrated. **e, f, g** Experiments show the response of a finite-difference control waveform built from a zeroth-order DPSS to a range of probe frequencies, f_{sid} , applied in the form of a single-frequency modulation in the dephasing quadrature. Measurements are taken in the x , y and z quadrature as the survival probability along the corresponding Bloch sphere projection. Experimental data is represented by markers, while continuous lines show numerical simulations. Each data point comprises an average over 500 individual repetitions of the experiment and the error bars represent the standard deviations of those averages. **i, j** show the estimated dephasing filters for control duration τ , $\hat{S}_i(\tau) = \langle |\hat{a}_i^{(1)}(\tau)|^2 \rangle \approx |\hat{F}_{zi}(\omega_{\text{sid}}, \tau)|^2$, $i \in \{y, z\}$, calculated from linear combinations of the projection data (inset equations). **h** consistently shows no sensitivity to dephasing noise in the signal's x projection, $S_x(\tau) = \langle |a_x^{(1)}(\tau)|^2 \rangle \approx |\hat{F}_{xx}(\omega_{\text{sid}}, \tau)|^2$. In **i** we recover the desired spectrally concentrated dephasing filter $F_z(\omega, \tau)$.

trated response to the dephasing signal, $\beta_z(t)$. We target the dephasing sensitivity of the y error-vector component, given in Eq. (2b), and the corresponding signal projection $S_y(t) \equiv \langle |a_y^{(1)}(t)|^2 \rangle$, given in Eq. (4b). Since the nonlinearity arises from both the sinusoidal dependence and the time-integral over $\Omega(t)$, this may be accomplished by linearizing the sine term, so that $\sin \Theta(t) \approx \Theta(t)$, and then by compensating the integral via “derivative control,” letting $\Omega(t) \mapsto \frac{d}{dt}\Omega(t)$ (see Fig. 1d). More formally, as DPSS are discrete-time sequences, we resort to a finite-difference modulation protocol. Let us for simplicity focus on achieving spectral concentration around zero frequency, and let $\Omega_{\text{DPSS}}(t) \equiv \Omega v_n^{(k)}(N, W)$, $\Omega > 0$, denote a k -th order DPSS, with bandwidth parameter W and sampling interval Δt , so that $t \in [n\Delta t, (n+1)\Delta t]$, $n = 0, 1, \dots, N-1$ [23]. Then finite-difference control is implemented by letting

$$\Omega_{\text{FD}}(t) \equiv \begin{cases} \Omega v_0^{(k)}(N, W), \\ \Omega [v_1^{(k)}(N, W) - v_0^{(k)}(N, W)], \\ \vdots \\ \Omega [v_{N-1}^{(k)}(N, W) - v_{N-2}^{(k)}(N, W)]. \end{cases} \quad (5)$$

Remarkably, direct calculation shows that, under the above protocol, not only does the dephasing FF, $F_z(\omega, t)$, recover

the desired spectral concentration, but concentration is also retained for the amplitude FF, $F_\Omega(\omega, t)$. In addition, finite-difference control can easily be made compatible with the analog modulation techniques that are needed to shift the filter passband [22, 23] (see Supplementary Note 2 for full detail).

Experimental implementation and validation. We experimentally demonstrate the above concepts using a sensor based on a single $^{171}\text{Yb}^+$ ion in a linear Paul trap. The qubit is realized through the hyperfine splitting of the $^1S_{1/2}$ ground state with a transition frequency ~ 12.6 GHz [22, 30, 31]. To drive the transition and implement control along both σ_x and σ_y , we employ a vector signal generator with I/Q modulation to produce an effective control Hamiltonian $H_{\text{ctrl}}(t) = \Omega(t)[\cos \varphi(t)\sigma_x + \sin \varphi(t)\sigma_y]$. Here, $\Omega(t)$ is the driving amplitude given by the magnitude of the time-dependent I/Q components as $\Omega(t) = \sqrt{I^2(t) + Q^2(t)}$, and the control phase is given by the angle between them as $\varphi(t) = \tan[Q(t)/I(t)]$ (see also Supplementary Note 3).

Readout is performed through projective measurements in the z basis, where we label the states $|\uparrow_z\rangle \equiv |0\rangle$ and $|\downarrow_z\rangle \equiv |1\rangle$. All control waveforms used here implement a net identity operation, such that when we prepare a state in $|\uparrow_z\rangle$, we can represent the measured survival probability as $P(\uparrow_z, t) = \langle |\langle \uparrow_z | \tilde{U}(t) | \uparrow_z \rangle|^2 \rangle$. A three-axes measurement routine fol-

lowing application of control permits the ensemble-averaged error-vector components to be estimated via linear combinations of $P(\hat{\alpha}_i, t) \approx 1 - \langle |a_j^{(1)}(t)|^2 \rangle - \langle |a_k^{(1)}(t)|^2 \rangle$, for cyclic permutations of $i, j, k \in \{x, y, z\}$ (see [22], Supplementary Note 3, and [23]), as long as all components of $\mathbf{a}^{(1)}$ are sufficiently small [25, 28].

Using this three-axes measurement strategy, we demonstrate the narrowband selectivity of finite-difference DPSS controls by reconstructing the controlled sensor's spectral response. We begin by choosing an appropriately constructed DPSS control which is tuned using sinusoidal modulation to shift the target sensing band to 10 kHz [22]. We then employ frequency-selective system identification (sid) to map out the FFs in the presence of additive engineered dephasing noise. A weak, single-frequency disturbance at ω_{sid} is generated by a separate waveform generator and added to the frequency of the driving field via external frequency modulation. This creates an effective dephasing noise term $\beta_z(t)\sigma_z$, with $\beta_z(t) \propto \cos(\omega_{\text{sid}}t + \phi)$, where the variable phase ϕ is sampled linearly over $[0, 2\pi]$, in such a way that averaging over ϕ yields $S_z(\omega) \propto \delta(\omega - \omega_{\text{sid}})$ [31]. Leveraging the relationship between signal's projections and FFs yields the desired estimates, $\hat{S}_i(\tau) = \langle |\hat{a}_i^{(1)}(\tau)|^2 \rangle \approx |\hat{F}_{zi}(\omega_{\text{sid}}, \tau)|^2$, $i \in \{y, z\}$. Varying ω_{sid} and averaging over ϕ for each value of ω_{sid} then allows direct reconstruction of the FF vs probe frequency.

Data for all Cartesian projections of the measured sensor state are presented in Fig. 1e-g. We observe that all projections exhibit sensitivity to the system-identification stimulus, and all show structure outside of the shaded region representing the target band. However, on inverting these data to reconstruct the FFs, $\hat{S}_y(\tau) \approx \hat{F}_z(\omega, \tau)$ reveals spectral concentration in the target band with minimal measured leakage, as intended. The target band is user-defined and experiments performed with different DPSS orders and band shifts reveal comparable performance. In all cases, data agree well with numerical simulations, and the data appearing in Fig. 1i constitute the key validation of our approach to control design.

Dephasing noise spectroscopy. We now demonstrate the reconstruction of a noise spectrum resulting from an additive dephasing term $\beta_z(t)$ as in Eq. (1). Specifically, we engineer a complex, “mixed” spectrum that exhibits both a broadband $1/f$ component and discrete, narrowband spectral features. This spectrum is converted to a time-domain disturbance through an inverse Fourier transform and applied to the sensor via frequency modulation of the driving field, which is physically equivalent to an ambient dephasing field [31, 32]. Spectral reconstruction begins with application of appropriate finite-difference DPSS controls and execution of the above tomographic measurement protocol.

Following the two-stage estimation procedure proposed in [23], we first perform a coarse sampling in frequency aimed to detect the presence of spectral structure, by using controls of duration $\tau = N\Delta t = 2.5$ ms and bandwidth product $NW = 4$, thereby achieving an effective sample bandwidth of $f_B \equiv NW/\tau = 1.6$ kHz. If $\omega_s = 2\pi f_s$ is the band-shift

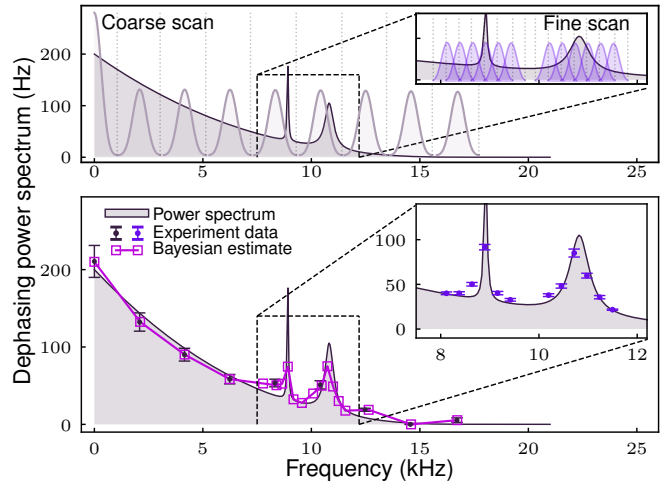


FIG. 2. Dephasing noise spectrum reconstruction. **a** shows the engineered power spectrum on the left axis, along with the FFs used for the reconstruction. Controls comprised of zeroth-order DPSS with duration $\tau = 2.5$ ms, bandwidth product $NW = 4$, and band-shift frequencies $f_s = 0, 2.1, 4.2, 6.2, 8.3, 10.4, 12.5, 14.6, 16.7$ kHz. The inset shows the location of the filters used in the fine scan, again with zeroth-order DPSS, but now 5 ms long with $NW = 2$ and $f_s = 8.1, 8.4, 8.6, 8.9, 9.2, 9.4, 9.9, 10.2, 10.5, 10.9, 11.2, 11.5$ kHz. **b** shows the experimental spectrum reconstruction of both the coarse (main panel) and fine (inset) scan. Experiments are averaged over 400 time-domain realizations of the noise spectrum and error bars represent the variance over outcomes. A Bayesian update is employed to combine data from both scans and obtain the final estimate.

frequency, the resulting dephasing FFs are spectrally concentrated in a passband $B_s \equiv (\omega_s - 2\pi f_B, \omega_s + 2\pi f_B)$. Using the spectral concentration of the FFs to truncate the integral in Eq. (4b) and assuming that $S_z(\omega)$ is locally flat in B_s , the dephasing spectrum is inferred from experimentally determined values of $\hat{S}_y(\tau)$ using the relationship $\hat{S}_z(\omega_s) \approx \pi \hat{S}_y(\tau) / \int_{B_s} d\omega F_z(\omega, \tau)$. We then supplement this initial coarse estimate of the spectrum with a fine scan, using enhanced spectral resolution in a region where prominent features deviating from a smooth trend are observed; this is achieved by adjusting the control duration to $\tau = 5$ ms and letting $NW = 2$ to achieve $f_B = 0.4$ kHz (Fig. 2a). A Bayesian update (see Supplementary Note 4) is then used to combine the information from the coarse and fine scans to find the most likely spectral weight across the measurement range. Our experimental measurements and the associated reconstructions, shown in Fig. 2, provide both quantitative and qualitative agreement with the applied noise spectrum using no free parameters. We further provide a comparative analysis of the performance of our DPSS protocol against standard CPMG-based sensing in Supplementary Note 5.

Simultaneous multi-axis sensing. We now address the challenge of multi-axis reconstruction of simultaneous, but statistically independent noise spectra, $S_\Omega(\omega)$ and $S_z(\omega)$; a scenario that is commonly encountered for sensors in which the driven control itself suffers from imperfections. Both spectra

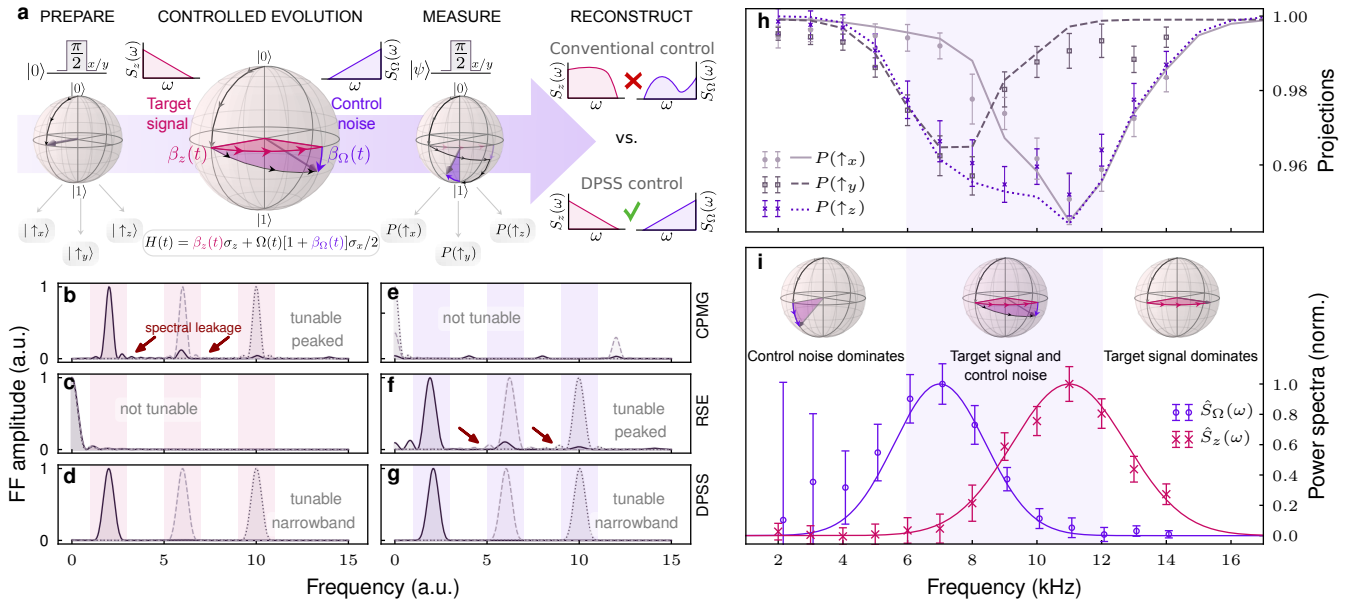


FIG. 3. Multi-axis sensing of time-dependent signals with a qubit sensor. **a** illustrates the four stages of the sensing process. $\pi/2$ pulses are employed to prepare the qubit in the $+x$, $+y$ and $+z$ state of the Bloch sphere. The qubit is then subjected to a driving field that probes two time-dependent signals, $\beta_z(t)$ and $\beta_\Omega(t)$, in the target dephasing ($\propto \sigma_z$) and the control ($\propto \sigma_x$) quadrature. Combining measurements in all three axes enables the spectral reconstruction of both signals. **b**, **c**, **d** show the sensitivity to the target dephasing signal, β_z , for CPMG control, rotary spin echoes (RSE) and DPSS, by means of the dephasing FFs at three different probe frequencies. **e**, **f**, **g** show the corresponding FFs in the control quadrature, as a means to model sensitivity to β_Ω . Filters have been scaled to the same amplitude for display purposes. Only for the DPSS controls the corresponding FFs are concentrated in both quadratures. **h**, **i** show the simultaneous experimental reconstruction of an engineered dephasing spectrum, $S_z(\omega)$, and an engineered control noise spectrum, $S_\Omega(\omega)$, that partly overlap in frequency space. Inset Bloch spheres show the effective rotation of a qubit state prepared in either $+x$ or $+y$ on the Bloch vector in three distinct frequency regions, which are separated by shaded regions indicating the spectral overlap between $S_z(\omega)$ and $S_\Omega(\omega)$. **h** Projective measurement data for each control waveform as a function of probe frequency. The error bars represent the variance over 100 individual time-domain noise realizations. Lines represent numerical simulations. **i** shows the reconstructed power spectra in both quadratures. The spectra and data have been normalized for display purposes, original spectrum amplitudes were $S_\Omega^{(\max)}(\omega) \approx 450$ Hz and $S_z^{(\max)}(\omega) \approx 15$ Hz.

contribute to the evolution of the sensor's state, making direct spectral estimation from single-axis measurements difficult. Figure 3a schematically represents the measurement process including state preparation, controlled evolution, three-axis measurement and finally spectral reconstruction. Conventional control protocols struggle to accurately perform the final reconstruction because they are designed to be spectrally concentrated and tunable in at most one quadrature at a time (Fig. 3b/e and c/f). In contrast, our finite-difference DPSS control, while being designed to ensure spectrally concentrated sensitivity to dephasing noise $\propto \sigma_z$, has the additional benefit that spectral concentration is also preserved for multiplicative control noise along $\propto \sigma_x$. As a result, we see in Fig. 3b-g that, when compared to other common sensing protocols, *only* the finite-difference DPSS modulation yields FFs which are simultaneously concentrated for both noise sources, thus enabling multi-axis spectral estimation. Specifically, this may be achieved by inferring the dephasing spectrum from $\hat{S}_y(\omega)$, as previously described, and similarly inferring the amplitude spectrum by $\hat{S}_\Omega(\omega_s) \approx \pi \hat{S}_x(\tau) / \int_{B_s} d\omega F_\Omega(\omega, \tau)$.

To experimentally validate this approach, we engineer two Gaussian-shaped power spectral densities for both $S_\Omega(\omega)$ and

$S_z(\omega)$, which partly overlap in frequency (shaded region, Fig. 3i). Again, these spectra are converted to time-domain disturbances and applied to the sensor. We then perform tomographic measurements under application of these disturbances using finite-difference DPSS controls at $M = 13$ different band-center frequencies (see Fig. 3h). Reconstructions based on the tomographic measurements obtained under simultaneous application of both noise spectra are shown in Fig. 3i. Data agree well with the applied noise spectra, including in the central frequency band of 6 – 12 kHz, where both spectra contribute approximately equally to the overall sensor response. The larger error bars appearing for low frequency values arise due to uncertainty introduced by the fact that the amplitude-filter magnitude diminishes with reduced band-shift frequency ω_s (see Supplementary Note 2). The magnitude of the dephasing filters, on the other hand, is kept constant throughout the frequency scan range. Again, we stress that there are no free parameters used in representing the solid lines presented in Fig. 3i.

Discussion

In summary, we demonstrated the implementation of a continuously driven control protocol for quantum sensing which exhibits optimal spectral concentration in the dephasing quadrature $\propto \sigma_z$, for controls driven in σ_x or σ_y , as is the typical setting in many sensing applications. The continuous nature of these controls offers superior flexibility compared to standard pulsed control and the resolution of the reconstruction is arbitrarily tunable (subject to sampling resolution of the arbitrary waveform generators). Additionally, our controls exhibit spectral concentration in both the dephasing and control quadrature simultaneously and can therefore be employed to produce a minimally biased sensor in applications that suffer from time-dependent control noise which distorts the target dephasing signal. This allows for simultaneous, multi-axis spectral estimation of both the control noise and the dephasing noise power spectral densities.

Future work will see the extension of our protocol to different Hamiltonian models for the interaction between control and noise – in particular, the case of control noise which couples additively as encountered with cross-talk. Furthermore, we will consider different models for the noise that relax assumptions about the noise process, to include *e.g.*, non-classical [10] or non-Gaussian noise [7, 33] in both the control and dephasing quadrature. Finally, we are interested in designing controls and filters for multi-qubit operations to sense noise and unwanted cross-talk across an array of qubits, in order to perform spatial as well as temporal noise reconstruction, both of which would leverage the spectrally concentrated properties of the DPSS control sequences.

Acknowledgements. It is a pleasure to thank D. Lucarelli for pointing us towards the DPSS and for helpful discussions, and S. Mavadia for early contributions, in particular to pulsed DPSS protocols. We also acknowledge J. Wakulicz and A. Singh for assisting in the experimental data acquisition process. This work was partially supported by the ARC Centre of Excellence for Engineered Quantum Systems CE110001013, the US Army Research Office under Contract W911NF-12-R-0012, IARPA via Department of Interior National Business Center contract number 2012-12050800010, and a private grant from H. & A. Harley.

Author contributions. V. F. developed experimental hardware, built the experimental control system, and obtained the presented data with theoretical techniques developed by L.M.N. and L.V.. Numerical simulations and data analysis were performed by V. F., L.M.N., and L.V. M.J.B. conceived the experiment and led development of the experimental system. V. F., L.M.N., L.V., and M.J.B. jointly wrote the manuscript.

Additional information. Experimental and numerically simulated data, as well as simulation code are available from the authors upon request.

- * Contact: michael.biercuk@sydney.edu.au
- [1] C. L. Degen, F. Reinhard, and P. Cappellaro, “Quantum sensing,” *Rev. Mod. Phys.*, vol. 89, p. 035002, Jul (2017).
 - [2] G. A. Álvarez and D. Suter, “Measuring the spectrum of colored noise by dynamical decoupling,” *Phys. Rev. Lett.*, vol. 107, p. 230501, (2011).
 - [3] J. Bylander, S. Gustavsson, F. Yan, F. Yoshihara, K. Harrabi, G. Fitch, D. G. Cory, Y. Nakamura, J. S. Tsai, and W. D. Oliver, “Noise spectroscopy through dynamical decoupling with a superconducting flux qubit,” *Nat. Phys.*, vol. 7, pp. 565–570, (2011).
 - [4] J. Taylor, P. Cappellaro, L. Childress, L. Jiang, D. Budker, P. Hemmer, A. Yacoby, R. Walsworth, and M. Lukin, “High-sensitivity diamond magnetometer with nanoscale resolution,” *Nat. Phys.*, vol. 4, pp. 810–816, (2008).
 - [5] A. Stark, N. Aharon, T. Unden, D. Louzon, A. Huck, A. Retzker, U. L. Andersen, and F. Jelezko, “Narrow-bandwidth sensing of high-frequency fields with continuous dynamical decoupling,” *Nat. Commun.*, vol. 8, p. 1105, (2017).
 - [6] K. Mizuno, M. Nakajima, H. Ishiwata, Y. Masuyama, T. Iwasaki, and M. Hatano, “Wide-field diamond magnetometry with millihertz frequency resolution and nanotesla sensitivity,” *AIP Advances*, vol. 8, p. 125316, (2018).
 - [7] L. M. Norris, G. A. Paz-Silva, and L. Viola, “Qubit noise spectroscopy for non-Gaussian dephasing environments,” *Phys. Rev. Lett.*, vol. 116, p. 150503, (2016).
 - [8] M. Hirose, C. D. Aiello, and P. Cappellaro, “Continuous dynamical decoupling magnetometry,” *Phys. Rev. A*, vol. 86, p. 062320, (2012).
 - [9] F. Yan, S. Gustavsson, J. Bylander, X. Jin, F. Yoshihara, D. G. Cory, Y. Nakamura, T. P. Orlando, and W. D. Oliver, “Rotating-frame relaxation as a noise spectrum analyser of a superconducting qubit undergoing driven evolution,” *Nat. Commun.*, vol. 4, p. 2337, (2013).
 - [10] F. Yan, D. Campbell, P. Krantz, M. Kjaergaard, D. Kim, J. L. Yoder, D. Hover, A. Sears, A. J. Kerman, T. P. Orlando, S. Gustavsson, and W. D. Oliver, “Distinguishing coherent and thermal photon noise in a circuit quantum electrodynamical system,” *Phys. Rev. Lett.*, vol. 120, p. 260504, (2018).
 - [11] G. A. Paz-Silva, L. M. Norris, F. Beaudoin, and L. Viola, “Extending comb-based spectral estimation to multiaxis quantum noise,” *Phys. Rev. A*, vol. 100, p. 042334, (2019).
 - [12] H. Y. Carr and E. M. Purcell, “Effects of diffusion on free precession in nuclear magnetic resonance experiments,” *Phys. Rev.*, vol. 94, pp. 630–638, (1954).
 - [13] S. Meiboom and D. Gill, “Modified spin echo method for measuring nuclear relaxation times,” *Review of Scientific Instruments*, vol. 29, no. 8, pp. 688–691, (1958).
 - [14] L. Viola, E. Knill, and S. Lloyd, “Dynamical decoupling of open quantum systems,” *Phys. Rev. Lett.*, vol. 82, pp. 2417–2421, (1999).
 - [15] C. D. Aiello, M. Hirose, and P. Cappellaro, “Composite-pulse magnetometry with a solid-state quantum sensor,” *Nat. Commun.*, vol. 4, p. 1419, (2013).
 - [16] H. Ball and M. J. Biercuk, “Walsh-synthesized noise filters for quantum logic,” *EPJ Quantum Tech.*, vol. 2, p. 11, (2015).
 - [17] M. Loretz, T. Rosskopf, J. M. Boss, S. Pezzagna, J. Meijer, and C. L. Degen, “Single-proton spin detection by diamond magnetometry,” *Science*, (retracted), (2014).
 - [18] M. Loretz, J. M. Boss, T. Rosskopf, H. J. Mamin, D. Rugar, and C. L. Degen, “Spurious harmonic response of multipulse

- quantum sensing sequences,” *Phys. Rev. X*, vol. 5, p. 021009, (2015).
- [19] D. Slepian, “Some comments on Fourier analysis, uncertainty and modeling,” *Society for Industrial and Applied Mathematics*, vol. 25, pp. 379–393, (1983).
- [20] D. B. Percival and A. T. Walden, *Spectral Analysis for Physical Applications*. Cambridge University Press, (1993).
- [21] D. Lucarelli, “Quantum optimal control via gradient ascent in function space and the time-bandwidth quantum speed limit,” *Phys. Rev. A*, vol. 97, p. 062346, (2018).
- [22] V. Frey, S. Mavadia, L. M. Norris, W. de Ferranti, D. Lucarelli, L. Viola, and M. J. Biercuk, “Application of optimal band-limited control protocols to quantum noise sensing,” *Nat. Commun.*, vol. 8, p. 2189, (2017).
- [23] L. M. Norris, D. Lucarelli, V. M. Frey, S. Mavadia, M. J. Biercuk, and L. Viola, “Optimally band-limited spectroscopy of control noise using a qubit sensor,” *Phys. Rev. A*, vol. 98, p. 032315, (2018).
- [24] A. G. Kofman and G. Kurizki, “Unified theory of dynamically suppressed qubit decoherence in thermal baths,” *Phys. Rev. Lett.*, vol. 93, p. 130406, (2004).
- [25] T. J. Green, J. Sastrawan, H. Uys, and M. J. Biercuk, “Arbitrary quantum control of qubits in the presence of universal noise,” *New J. Phys.*, vol. 15, p. 095004, (2013).
- [26] H. Ball and M. J. Biercuk, “Walsh-synthesized noise filters for quantum logic,” *EPJ Quantum Tech.*, vol. 2, (2015).
- [27] G. A. Paz-Silva and L. Viola, “General transfer-function approach to noise filtering in open-loop quantum control,” *Phys. Rev. Lett.*, vol. 113, p. 250501, (2014).
- [28] A. Soare, H. Ball, D. Hayes, J. Sastrawan, M. C. Jarrat, J. J. McLoughlin, X. Zhen, T. Green, and M. J. Biercuk, “Experimental noise filtering by quantum control,” *Nat. Phys.*, vol. 10, pp. 825–829, (2014).
- [29] K. Khodjasteh and L. Viola, “Dynamically error-corrected gates for universal quantum computation,” *Phys. Rev. Lett.*, vol. 102, p. 080501, (2009).
- [30] S. Mavadia, V. Frey, J. Sastrawan, S. Dona, and M. J. Biercuk, “Prediction and real-time compensation of qubit decoherence via machine learning,” *Nat. Commun.*, vol. 8, p. 14106, (2017).
- [31] A. Soare, H. Ball, D. Hayes, X. Zhen, M. C. Jarrat, J. Sastrawan, H. Uys, and M. J. Biercuk, “Experimental bath engineering for quantitative studies of quantum control,” *Phys. Rev. A*, vol. 89, p. 042329, (2014).
- [32] H. Ball, W. D. Oliver, and M. J. Biercuk, “The role of master clock stability in quantum information processing,” *NPJ Quantum Inf.*, vol. 2, p. 16033, (2016).
- [33] Y. Sung, F. Beaudoin, L. M. Norris, F. Yan, D. K. Kim, J. Y. Qiu, U. von Lüepke, J. L. Yoder, T. P. Orlando, L. Viola, S. Gustavsson, and W. D. Oliver, “Non-Gaussian noise spectroscopy with a superconducting qubit sensor,” *Nat. Commun.*, vol. 10, p. 3715, (2019).
- [34] D. J. Thomson, “Spectrum estimation and harmonic analysis,” *Proceedings of the IEEE*, vol. 70, pp. 1055–1096, (1982).
- [35] A. Tikhonov, “Solution of incorrectly formulated problems and the regularization method,” *Dokl. Akad. Nauk.*, vol. 151, pp. 1035–1038, (1963).
- [36] L. M. Norris, G. A. Paz-Silva, and L. Viola, “Qubit noise spectroscopy for non-gaussian dephasing environments,” *Phys. Rev. Lett.*, vol. 116, p. 150503, (2016).
- [37] P. Szańkowski, G. Ramon, J. Krzywda, D. Kwiatkowski, and Ł. Cywiński, “Environmental noise spectroscopy with qubits subjected to dynamical decoupling,” *J. Phys.: Condensed Matter*, vol. 29, no. 33, p. 333001, (2017).

Supplementary Information: Optimally band-limited controls for quantum multi-axis spectral estimation

Supplementary Note 1: Filter function formalism for DPSS control modulation

As noted in the main text, amplitude and dephasing noise enter the qubit dynamics, respectively, through the quantities

$$\langle |a_x^{(1)}(\tau)|^2 \rangle = \left\langle \left| \frac{1}{2} \int_0^\tau ds \Omega(s) \beta_\Omega(s) \right|^2 \right\rangle = \frac{1}{\pi} \int_0^\infty d\omega F_\Omega(\omega, \tau) S_\Omega(\omega), \quad (6)$$

$$\langle |a_y^{(1)}(\tau)|^2 \rangle = \left\langle \left| \int_0^\tau ds \sin \Theta(s) \beta_z(s) \right|^2 \right\rangle = \frac{1}{\pi} \int_0^\infty d\omega F_z(\omega, \tau) S_z(\omega), \quad (7)$$

where $S_i(\tau) \equiv \langle |a_i^{(1)}(\tau)|^2 \rangle$ is the “signal projection” onto the axis i and $^{(1)}$ indicates the first-order approximation of the Magnus expansion. Since we are only working with this order, the superscript is dropped in the following derivations for notational convenience. In the above expressions, the amplitude filter function (FF), $F_\Omega(\omega, \tau) \equiv |F_{xx}(\omega, \tau)|^2/4$, and the dephasing FF, $F_z(\omega, \tau) \equiv |F_{zy}(\omega, \tau)|^2$, are frequency-domain representations of the applied control, which depend on the first order FFs,

$$F_{xx}(\omega, \tau) \equiv \int_0^\tau ds e^{i\omega s} \Omega(s), \quad (8)$$

$$F_{zy}(\omega, \tau) \equiv \int_0^\tau ds e^{i\omega s} \sin \Theta(s), \quad \Theta(t) \equiv \int_0^t ds \Omega(s). \quad (9)$$

The linear dependence of the integrand in Eq. (8) on $\Omega(t)$ makes it possible to generate optimally bandlimited amplitude FFs by simply applying an amplitude control waveform proportional to a DPSS. Specifically, Refs. [22] and [23] considered an amplitude control waveform divided into N piecewise constant increments of duration Δt with $\tau = N\Delta t$,

$$\Omega_{\text{DPSS}}(t) = \Omega v_n^{(k)}(N, W), \quad t \in [n\Delta t, (n+1)\Delta t], \quad n = 0, 1, \dots, N-1, \quad (10)$$

where $\{v_n^{(k)}(N, W)\}$ is a DPSS of order k and Ω is a scaling factor in units of frequency. The frequency domain representation of $\{v_n^{(k)}(N, W)\}$ is known as a discrete prolate spheroidal wavefunction (DPSWF),

$$U^{(k)}(N, W; \omega) \equiv \epsilon_k \sum_{n=0}^{N-1} v_n^{(k)}(N, W) e^{i\omega[n-(N-1)/2]\Delta t}, \quad (11)$$

where $\epsilon_k = 1$ (i) for even (odd) k . The DPSWF $U^{(k)}(N, W; \omega)$ has the property of being spectrally concentrated in a frequency band $B_0 \equiv (-2\pi W/\Delta t, 2\pi W/\Delta t)$, centered at $\omega = 0$. Using Eq. (11), we see that the basic DPSS modulation described above produces the amplitude FF

$$F_\Omega(\omega, \tau) = \frac{\Omega^2 \sin^2(\omega \Delta t/2)}{\omega^2} U^{(k)}(N, W; \omega)^2.$$

This FF inherits the spectral concentration properties of $U^{(k)}(N, W; \omega)$, namely, it is also concentrated in the band B_0 . Its spectral concentration can be “shifted” in the frequency domain through signal processing techniques such as single-sideband or co-sinusoidal modulation [22, 23]. To shift the FF by a frequency $\omega_s \geq 0$ using sinusoidal modulation, the amplitude waveform in Eq. (10) is modified by

$$\Omega_{\text{cos}}(t) = \Omega \cos(n\omega_s \Delta t) v_n^{(k)}(N, W), \quad t \in \Delta t [n, n+1], \quad n = 0, 1, \dots, N-1. \quad (12)$$

In the positive half of the frequency domain, the resulting FF is then spectrally concentrated about ω_s

$$F_\Omega(\omega, \tau) \approx \frac{\Omega_s^2 \sin^2(\omega \Delta t/2)}{2\omega^2} \left[|U^{(k)}(N, W; \omega - \omega_s)|^2 + |U^{(k)}(N, W; \omega + \omega_s)|^2 \right], \quad (13)$$

where the scaling factor Ω_s is chosen so that the integral $\int_0^T ds \Omega_{\text{cos}}(s)^2$ is the same for all ω_s . This expression for $F_\Omega(\omega, \tau)$ holds when either $\omega_s = 0$ or $\omega_s > 2\pi W/\Delta t$. When $0 < \omega_s \leq 2\pi W/\Delta t$, alternative modulation techniques are required to avoid distortion of the filter [23].

Supplementary Note 2: DPSS finite-difference control modulation

1. Finite-difference control protocol

While simple DPSS modulation produces spectrally concentrated amplitude FFs, the nonlinear dependence on $\Omega(t)$ in the integrand of Eq. (9) prevents the same procedure from working for dephasing. Under the assumption that $\Theta(t) \ll \pi/2$, we can linearize the sine function in Eq. (9),

$$F_{zy}(\omega, \tau) \approx \int_0^\tau ds e^{i\omega s} \Theta(s). \quad (14)$$

Since $\Theta(t) = \int_0^t ds \Omega(s)$, it follows that we can create a spectrally concentrated dephasing FF, taking a form similar to Eq. (13), by using an amplitude waveform $\Omega(t) \propto \frac{d}{dt} \Omega_{\text{cos}}(t)$. As $\Omega_{\text{cos}}(t)$ is piece-wise constant, however, this time derivative does not exist. Instead, we use an amplitude waveform depending on the finite difference of $\Omega_{\text{cos}}(t)$, the discrete analogue of a derivative. If $V_n \equiv \Omega \cos(n\omega_s \Delta t) v_n^{(k)}(N, W)$ is shorthand for the piecewise-constant increments of $\Omega_{\text{cos}}(s)$, the finite-difference waveform is given by

$$\Omega_{\text{FD}}(t) = \begin{cases} V'_0 \equiv V_0, & t \in \Delta t [0, 1) \\ V'_1 \equiv V_1 - V_0, & t \in \Delta t [1, 2) \\ V'_2 \equiv V_2 - V_1, & t \in \Delta t [2, 3) \\ \vdots & \vdots \\ V'_{N-1} \equiv V_{N-1} - V_{N-2}, & t \in \Delta t [N-2, N-1]. \end{cases} \quad (15)$$

Under this amplitude modulation, observe that the rotation angle at $t = m\Delta t$ becomes

$$\Theta(m\Delta t) = \int_0^{m\Delta t} ds \Omega_{\text{FD}}(s) = \sum_{n=0}^{m-1} V'_n \Delta t = V_{m-1} \Delta t = \Omega \Delta t \cos[(m-1)\omega_s \Delta t] v_{m-1}^{(k)}(N, W).$$

At each time increment, the rotation angle is proportional to $\Omega_{\text{cos}}(t)$, as desired.

2. Finite-difference filter functions

At an arbitrary time $t \in [0, \tau]$, not necessarily an integer multiple of Δt , the rotation angle generated by the finite-difference waveform is

$$\begin{aligned} \Theta(t) &\equiv \int_0^t ds \Omega_{\text{FD}}(s) = \int_{\lfloor \frac{t}{\Delta t} \rfloor \Delta t}^t ds \Omega_{\text{FD}}(s) + H(\lfloor t/\Delta t \rfloor - 1) \sum_{k=0}^{\lfloor \frac{t}{\Delta t} \rfloor - 1} \int_{k\Delta t}^{(k+1)\Delta t} ds \Omega'_{\text{FD}}(s) \\ &= V'_{\lfloor \frac{t}{\Delta t} \rfloor} (t - \lfloor t/\Delta t \rfloor \Delta t) + H(\lfloor t/\Delta t \rfloor - 1) \sum_{k=0}^{\lfloor \frac{t}{\Delta t} \rfloor - 1} V'_k \Delta t, \end{aligned}$$

where $\lfloor t/\Delta t \rfloor$ denotes the greatest integer less than or equal to $t/\Delta t$, and $H(\cdot)$ denotes the discrete Heaviside step function which is defined by

$$H(n) = \begin{cases} 0, & n < 0, \\ 1, & n \geq 0. \end{cases}$$

Using the relationship between the V_m and V'_m in Eq. (15), we obtain

$$\Theta(t) = V_{\lfloor \frac{t}{\Delta t} \rfloor} (t - \lfloor t/\Delta t \rfloor \Delta t) - H(\lfloor t/\Delta t \rfloor - 1) V_{\lfloor t/\Delta t \rfloor - 1} (t - \lceil t/\Delta t \rceil \Delta t), \quad (16)$$

where $\lceil t/\Delta t \rceil$ is the least integer greater than or equal to $t/\Delta t$. Substituting Eq. (16) into Eq. (14) and discretizing the time

integral yields

$$\begin{aligned}
F_{zy}(\omega, N\Delta t) &= \sum_{m=0}^{N-1} \int_{m\Delta t}^{(m+1)\Delta t} dt e^{i\omega t} \Theta(t) \\
&= \sum_{m=0}^{N-1} V_m \int_{m\Delta t}^{(m+1)\Delta t} dt e^{i\omega t} (t - m\Delta t) - \sum_{m=1}^{N-1} V_{m-1} \int_{m\Delta t}^{(m+1)\Delta t} dt e^{i\omega t} [t - (m+1)\Delta t] \\
&= \sum_{m=0}^{N-1} e^{i\omega m \Delta t} V_m \int_0^{\Delta t} dt [t + e^{i\omega \Delta t} (\Delta t - t)] - e^{i\omega N \Delta t} V_{N-1} \int_0^{\Delta t} dt e^{i\omega t} (\Delta t - t) \\
&= e^{i\omega[(N-1)/2]\Delta t} \tilde{V}(\omega) \int_0^{\Delta t} dt [t + e^{i\omega \Delta t} (\Delta t - t)] + \mathcal{O}(V_{N-1}) \\
&= e^{i\omega[(N-1)/2]\Delta t} \tilde{V}(\omega) \frac{(e^{i\Delta t \omega} - 1)^2}{\omega^2} + \mathcal{O}(V_{N-1}).
\end{aligned}$$

Here, the tilde denotes the discrete-time Fourier transform, i.e., for a discrete sequence $\{\Omega_n\}$,

$$\tilde{\Omega}(\omega) \equiv \sum_{n=0}^{N-1} \Omega_n e^{i\omega[n-(N-1)/2]\Delta t}.$$

Since $V_{N-1} \approx 0$ when $N \gg 1$ for a typical DPSS sequence,

$$\begin{aligned}
F_z(\omega, \tau) = |F_{zy}(\omega, N\Delta t)|^2 &= \frac{16 \sin^4(\omega \Delta t / 2)}{\omega^4} |\tilde{V}(\omega)|^2 + \mathcal{O}(V_{N-1}) \\
&\approx \frac{8 \Omega_s^2 \sin^4(\omega \Delta t / 2)}{\omega^4} \left[|U^{(k)}(N, W; \omega - \omega_s)|^2 + |U^{(k)}(N, W; \omega + \omega_s)|^2 \right], \quad (17)
\end{aligned}$$

where we have taken $\Omega \mapsto \Omega_s$. The resulting dephasing FF takes a form similar to the amplitude FF under simple DPSS and COS modulation in Eq. (13).

To determine the amplitude FF under finite-difference modulation, we follow a similar procedure. Discretizing the integral in Eq. (8) and substituting the finite-difference waveform in Eq. (15) for $\Omega(t)$ produces

$$\begin{aligned}
F_{xx}(\omega, N\Delta t) &= \sum_{m=0}^{N-1} \int_{m\Delta t}^{(m+1)\Delta t} dt e^{i\omega t} V'_m = \left[V_0 + \sum_{m=1}^{N-1} e^{i\omega m \Delta t} (V_m - V_{m-1}) \right] \int_0^{\Delta t} dt e^{i\omega t} \\
&= \left[e^{i\omega[(N-1)/2]\Delta t} (1 - e^{i\omega \Delta t}) \tilde{V}(\omega) + e^{i\omega N \Delta t} V_{N-1} \right] \int_0^{\Delta t} dt e^{i\omega t} \\
&= e^{i\omega[(N-1)/2]\Delta t} \frac{i(-1 + e^{i\Delta t \omega})^2}{\omega} \tilde{V}(\omega) + \mathcal{O}(V_{N-1}).
\end{aligned}$$

The amplitude FF is given by the square modulus of $F_{xx}(\omega, N\Delta t) = F_{xx}(\omega, \tau)$, which produces

$$\begin{aligned}
F_\Omega(\omega, \tau) &= |F_{xx}(\omega, \tau)|^2 / 4 \\
&= \frac{4 \sin^4(\omega \Delta t / 2)}{\omega^2} |\tilde{V}(\omega)|^2 + \mathcal{O}(V_{N-1}) \\
&\approx \frac{2 \Omega_s^2 \sin^4(\omega \Delta t / 2)}{\omega^2} \left[|U^{(k)}(N, W; \omega - \omega_s)|^2 + |U^{(k)}(N, W; \omega + \omega_s)|^2 \right]. \quad (18)
\end{aligned}$$

To leading order in V_{N-1} , observe that the amplitude FF differs from the dephasing FF in Eq. (17) by a factor of $4/\omega^2$.

3. Finite-difference control with embedded dynamical decoupling

As previously discussed, when truncating the Magnus expansion to the first order is viable, we can obtain the signal projection via projective measurements along three-axes, via $\mathcal{S}_y(\tau) \approx [1 + P(\hat{\gamma}_y, \tau) - P(\hat{\gamma}_x, \tau) - P(\hat{\gamma}_z, \tau)]/2$. Beyond the weak noise

limit, however, this procedure is complicated by the presence of higher-order terms in the Magnus expansion. Specifically,

$$\frac{1 + P(\uparrow_y, \tau) - P(\uparrow_x, \tau) - P(\uparrow_z, \tau)}{2} \approx \mathcal{S}_y(\tau) + 2\langle a_y^{(1)}(\tau) a_y^{(3)}(\tau) \rangle - \frac{1}{3} \langle a_y^{(1)}(\tau)^2 a_z^{(1)}(\tau)^2 \rangle, \quad (19)$$

where we have shown terms up to order τ^4 . Fortunately, the higher-order terms above depend on functionals of the form $\int_0^\tau ds (\cdot) \cos \Theta(s)$, which are absent in $\mathcal{S}_y(\tau)$, as seen in Eq. (7). Observe that under the transformation $\Theta(t) \mapsto \pi - \Theta(t)$, $\cos \Theta(t) \mapsto -\cos \Theta(t)$ whereas $\sin \Theta(t) \mapsto \sin \Theta(t)$. As we show below, this allows for the possibility to suppress the higher-order terms through dynamical decoupling targeted at $\cos \Theta(t)$, while preserving $\mathcal{S}_y(\tau)$.

For N such that $N/4$ is an integer, consider the following modified version of the finite-difference waveform in Eq. (15):

$$\Omega(t) = \begin{cases} V'_0 \equiv V_0, & t \in \Delta t [0, 1), \\ V'_1 \equiv V_1 - V_0, & t \in \Delta t [1, 2), \\ \vdots & \vdots \\ V'_{N/4-1} \equiv V_{N/4-1} - V_{N/4-2}, & t \in \Delta t [N/4-2, N/4-1), \\ V'_{N/4} \equiv \pi/\Delta t - V_{N/4} - V_{N/4-1}, & t \in \Delta t [N/4-1, N/4), \\ V'_{N/4+1} \equiv V_{N/4} - V_{N/4+1}, & t \in \Delta t [N/4, N/4+1), \\ \vdots & \vdots \\ V'_{3N/4-1} \equiv V_{3N/4-2} - V_{3N/4-1}, & t \in \Delta t [3N/4-2, 3N/4-1), \\ V'_{3N/4-1} \equiv V_{3N/4} + V_{3N/4-1} - \pi/\Delta t, & t \in \Delta t [3N/4-1, 3N/4), \\ V'_{3N/4} \equiv V_{3N/4} - V_{3N/4+1}, & t \in \Delta t [3N/4, 3N/4+1), \\ \vdots & \vdots \\ V'_N \equiv V_N - V_{N-1}, & t \in \Delta t [N, N-1). \end{cases}$$

If $\Omega(t)$ is such that $\Theta(t) \ll \pi/2$ for all t , this waveform produces

$$\sin \Theta(m\Delta t) \approx V_{m-1}\Delta t, \quad \cos \Theta(m\Delta t) \approx \begin{cases} 1, & t \in \Delta t [0, N/4), \\ -1, & t \in \Delta t [N/4, 3N/4), \\ 1, & t \in \Delta t [3N/4, N]. \end{cases}$$

The first expression is characteristic of ordinary finite-difference modulation, while the second approximates the switching function of a CPMG sequence. Consequently, $\mathcal{S}_y(\tau)$ takes the form of Eq. (7), where $F_z(\omega, \tau)$ is a spectrally concentrated finite-difference filter, and the higher order terms in Eq. (19) are suppressed. Using a similar procedure, we can generate $\cos \Theta(t)$ with sign changes at some set of arbitrary times $\{m_1\Delta t, \dots, m_n\Delta t\}$, allowing for the possibility of higher-order decoupling sequences such as concatenated decoupling. When the higher-order terms in Eq. (19) are sufficiently suppressed, the signal projection can be directly obtained from the usual expression, $\mathcal{S}_y(\tau) \approx [1 + P(\uparrow_y, \tau) - P(\uparrow_x, \tau) - P(\uparrow_z, \tau)]/2$, to good approximation. In doing so, care should be taken to ensure that the presence of periodicities in the applied pulses control does not generate harmonic components which could re-introduce appreciable spectral leakage in the target frequency range of reconstruction.

Supplementary Note 3: Experimental platform

Our experimental testbed consists of a single trapped $^{171}\text{Yb}^+$ ion in a linear Paul trap with qubit transition realized through the hyperfine splitting of the $S_{1/2}$ ground state. State initialization and readout is performed optically using a 369 nm laser with 935 nm and 638 nm repump lasers. Typical readout fidelities are around 99.7%. More information about the optical and trap setup can be found in previous works [28, 30].

The qubit transition frequency is at ~ 12.6 GHz which we drive using the amplified output of the commercial Keysight E8267D vector signal generator (VSG). A waveguide-to-coax converter creates free space microwaves that are routed through one of the trap viewports to the ion. Typical π -times are about $30 - 40$ μs with T_2 times of 200 ms. The VSG allows for programmable, digital I/Q modulation of the carrier frequency, enabling arbitrary control in both the x - and y -axis of the Bloch sphere through the effective Hamiltonian $H_{\text{ctrl}}(t) = \Omega(t)[\cos \varphi(t)\sigma_x + \sin \varphi(t)\sigma_y]$. The driving amplitude, $\Omega(t)$, is set by the magnitude of the I and Q waveforms via $\Omega(t) = \sqrt{I^2(t) + Q^2(t)}$, and the angle between I and Q determines the phase $\varphi(t) = \tan[Q(t)/I(t)]$. It is our convention to let the I quadrature correspond to the x -quadrature (and equivalently the Q

quadrature to y), hence when $Q(t) = 0$ we say we are driving an x -rotation. The DPSS waveforms are calculated numerically on the experiment PC and then uploaded to the VSGs internal I/Q DACs. All waveforms in this work are symmetric about zero and implement an identity operation. Separate waveforms to implement fast $\pi/2$ rotations before and after the DPSS waveform to perform the three-axis measurement are concatenated with the DPSS waveforms on the VSG, yielding three I/Q waveform sequences for each DPSS.

For experiments with engineered noise, amplitude noise is generated digitally and added to the DPSS waveforms before the upload. Dephasing noise is added using a Keysight 33600A arbitrary waveform generator (AWG) that likewise produces an analog waveform from a digital input, which is then fed to the external frequency modulation (FM) input of the VSG. This effectively implements a dephasing noise term $\beta_z(t)\sigma_z$, where $\beta_z(t)$ is the waveform produced by the AWG. For the experiments mapping out FFs, as reported in Fig. 1 in the main text, $\beta_z(t)$ was implemented as a single-frequency sine-wave with variable phase ϕ , that was linearly sampled from 0 to 2π . Each point in the reconstruction consists of an average over five individual measurements taken with different values of ϕ , so that $\langle \beta_z(t)\beta_z(t') \rangle \propto \cos(\omega_{\text{sid}}(t-t'))$. For all other experiments that used engineered dephasing noise with a target spectrum $S_z^t(\omega)$, we used a waveform $\beta_z(t) \propto \sum_i \sqrt{S_z^t(\omega_i)} \cos(\omega_i t + \phi_i)$. Averaging over phases in the time-domain results in the frequency-domain spectrum $S_z(\omega) \propto \sum_i S_z^t(\omega_i) \delta(\omega - \omega_i)$. We call each $\beta_z(t)$ that is calculated with a fixed set of random phases $\{\phi_i\}$ a single “noise realization”.

Supplementary Note 4: Bayesian spectral reconstruction procedure

The two-step Bayesian spectral reconstruction depicted in Fig. 2 of the main text is based on a procedure for the detection of peaks and narrowband spectral features detailed in Ref. [23]. This procedure involves an initial detection stage, in which wide-band DPSS FFs are used for a coarse reconstruction of the target noise spectrum. Statistically significant peaks or bumps in the coarse reconstruction signify the presence of narrowband spectral features, which are resolved with a subsequent fine-sampling of the spectrum using narrowband DPSS FFs. Measurements from the initial detection state determine a prior estimate of the spectrum, which is updated based on the subsequent measurements using narrowband Slepian filters.

In the present experiment, finite-difference modulation was used to generate 9 wide-band (or “coarse”, c) $k = 0$ DPSS FFs, centered at $f_s = 0, 2.1, 4.2, 6.2, 8.3, 10.4, 12.5, 14.6, 16.7$ kHz [Fig. 2(a) of the main text]. We denote the wide-band FF centered at $\omega_s = 2\pi f_s$ by $F_z^{c,s}(\omega, \tau)$. For each ω_s , the signal projection is related to the dephasing spectrum and $F_z^{c,s}(\omega, \tau)$ by

$$\mathcal{S}_y^{c,s}(\tau) = \frac{1}{\pi} \int_0^\infty d\omega S_z(\omega) F_z^{c,s}(\omega, \tau) \approx \frac{1}{\pi} \int_{B_s} d\omega S_z(\omega) F_z^{c,s}(\omega, \tau), \quad (20)$$

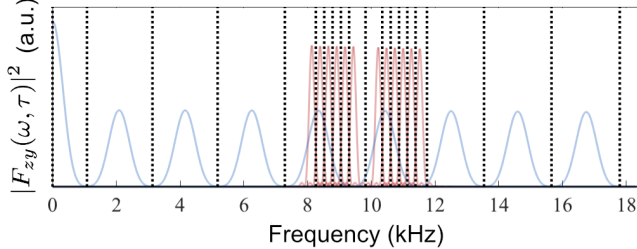
where we have used the fact that each FF is spectrally concentrated in a band $B_s \equiv (\max\{0, \omega_s - \Delta b\}, \omega_s + \Delta b)$ and $\Delta b \equiv 2\pi W/\Delta t$ to restrict the domain of integration in the second line. Using this expression, the spectrum at ω_s can be estimated by $\hat{S}(\omega_s) \equiv \hat{S}_y^{c,s}(\tau)/A_{c,s}$, where $\hat{S}_y^{c,s}(\tau)$ is the measured value of $\mathcal{S}_y^{c,s}(\tau)$ and $A_{c,s} \equiv \frac{1}{\pi} \int_{B_s} d\omega F_z^{c,s}(\omega, \tau)$. The estimate $\hat{S}(\omega_s)$, which is known as the $k = 0$ eigenestimate of the spectrum at ω_s , is in good agreement with the actual spectrum provided that $S_z(\omega)$ does not vary appreciably within B_s [23, 34]. The eigenestimates for each ω_s , plotted in Fig. 2(b) of the main text, closely match the actual spectrum at all frequencies except for the 8 – 12 kHz region, in which the spectrum has narrowband features and, consequently, varies significantly within B_s .

The two-step Bayesian procedure returns estimates of the spectrum in each of the 19 “segments” depicted in Fig. S1. The segments, which we denote by $\{\sigma_\ell | \ell = 1, \dots, 19\}$, are narrower in the 8 – 12 kHz region in order to resolve the spectral features absent in the initial eigenestimates. First, we determine the most probable estimate of the spectrum in the 19 segments based on the 9 original measurements of $\hat{S}_y^{c,s}(\tau)$ using the wide-band FFs. This will serve as a prior, which will be updated based on subsequent measurements. To establish the prior, we first discretize Eq. (20), which yields

$$\hat{S}_y^{c,s}(\tau) \approx \sum_{\ell=1}^{19} \frac{1}{\pi} \int_{\sigma_\ell} d\omega S_z(\omega) F_z^{c,s}(\omega, \tau) \approx \sum_{\ell=1}^{19} S_\ell \frac{1}{\pi} \int_{\sigma_\ell} d\omega F_z^{c,s}(\omega, \tau),$$

where S_ℓ is the average value of $S_z(\omega)$ in segment σ_ℓ . If we gather the values of $\hat{S}_y^{c,s}(\tau)$ for each wide-band filter into a 9×1 vector, \vec{S}_y^c , we can cast the expression above into a matrix equation

$$\vec{S}_y^c = \mathbf{F}^c \vec{S}, \quad (21)$$



Supplementary Figure S1. Frequency segments used in Bayesian procedure. Boundaries of the frequency segments (dotted lines) are depicted along with the wide-band dephasing filters (blue) and narrowband dephasing filters (red).

where $\vec{S} = (S_1, \dots, S_{19})^T$ and \mathbf{F}^c is a 9×19 “filter matrix” with elements depending on the wide-band FFs,

$$(\mathbf{F}^c)_{s,\ell} = \frac{1}{\pi} \int_{\sigma_\ell} d\omega F_z^{c,s}(\omega, \tau). \quad (22)$$

Since the linear system in Eq. (21) is underdetermined, we cannot solve for \vec{S} by straightforward linear inversion. Instead, we determine the prior mean through a regularized maximum likelihood estimate,

$$\vec{S}_0 = \operatorname{argmin}_{\vec{S}} \frac{1}{2} (\vec{S}_y^c - \mathbf{F}^c \vec{S})^T \Sigma_c^{-1} (\vec{S}_y^c - \mathbf{F}^c \vec{S}) + \|\lambda \mathbf{D}(\vec{S} - \bar{S})\|^2,$$

where Σ_c is the 9×9 covariance matrix with elements $(\Sigma_c)_{ss'} = \delta_{ss'} \operatorname{var}[\hat{S}_y^{c,s}]$. Note that the first term in this expression applies to a Gaussian likelihood function, valid in the limit of a large number of measurements. The rightmost term is an L_2 regularizer that ensures numerical stability [35], where $\lambda = 0.35$ is the strength of the regularization, \bar{S} is a constant 19×1 vector containing the mean of the initial eigenestimates and \mathbf{D} is a 19×19 diagonal matrix with nonzero elements, $D_{4,4} = \dots = D_{10,10} = 1$. The optimization has an analytic solution that yields the prior mean and corresponding covariance matrix,

$$\begin{aligned} \vec{S}_0 &= (\mathbf{F}^{cT} \Sigma_c^{-1} \mathbf{F}^c + 2\lambda^2 \mathbf{D}^2)^{-1} (\mathbf{F}^{cT} \Sigma_c^{-1} \vec{S}_y^c + 2\lambda^2 \mathbf{D}^2 \bar{S}), \\ \Sigma_0 &= (\mathbf{F}^{cT} \Sigma_c^{-1} \mathbf{F}^c + 2\lambda^2 \mathbf{D}^2)^{-1}. \end{aligned}$$

From these quantities, the prior distribution of \vec{S} is

$$P(\vec{S}) = \mathcal{N}_0 e^{\frac{1}{2}(\vec{S} - \vec{S}_0)^T \Sigma_0^{-1} (\vec{S} - \vec{S}_0)}, \quad (23)$$

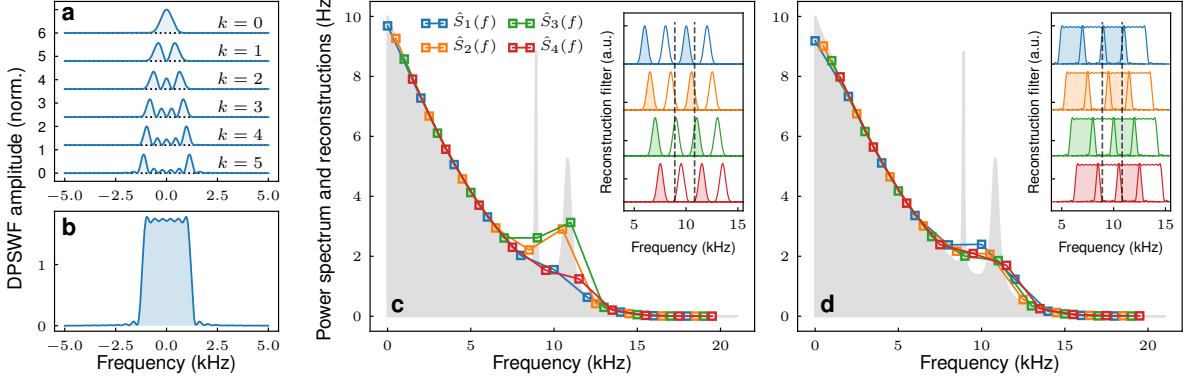
where \mathcal{N}_0 is a normalization constant. Note that the prior is Gaussian-distributed since the L_2 -regularizer preserves the Gaussianity of the likelihood function.

Next, we update the prior using data from additional measurements. To target the $8 - 12$ kHz region, the experiment used finite-difference sequences to generate 12 narrowband (or “fine”, f) $k = 0$ DPSS FFs. These FFs, centered at $\omega_s = 2\pi f_s$ with $f_s = 8.1, 8.4, 8.6, 8.9, 9.2, 9.4, 9.9, 10.2, 10.5, 10.9, 11.2, 11.5$ kHz, we denote by $F_z^{f,s}(\omega, \tau)$. In Fig. S1 above, observe that each of the smaller segments contain a single narrowband FF, while each of the larger segments contain a single wide-band FF. The measurements of $\mathcal{S}_y^{f,s}(\tau) \equiv \langle |a_y^{(1)}(\tau)|^2 \rangle$ for each $F_z^{f,s}(\omega, \tau)$ we gather into a vector $\vec{S}_y^f = [\hat{S}_y^{f,1}(\tau), \dots, \hat{S}_y^{f,12}(\tau)]^T$. The corresponding 12×12 covariance matrix has elements $(\Sigma_f)_{ss'} = \delta_{ss'} \operatorname{var}[\hat{S}_y^{f,s}]$. Define now the 12×19 filter matrix \mathbf{F}^f by $(\mathbf{F}^f)_{s,\ell} = \frac{1}{\pi} \int_{\sigma_\ell} d\omega F_z^{f,s}(\omega, \tau)$, in analogy to Eq. (22). The likelihood or conditional probability of measuring \vec{S}_y^f given the actual spectrum is then

$$P(\vec{S}_y^f | \vec{S}) = \mathcal{N} e^{\frac{1}{2}(\vec{S}_y^f - \mathbf{F}^f \vec{S})^T \Sigma_f^{-1} (\vec{S}_y^f - \mathbf{F}^f \vec{S})}.$$

Again, we have assumed that each entry of \vec{S}_y^f is Gaussian distributed in the limit of a large number of measurements. The posterior distribution is determined from the likelihood and prior in Eq. (23),

$$P(\vec{S} | \vec{S}_y^f) \propto P(\vec{S}_y^f | \vec{S}) P(\vec{S}).$$



Supplementary Figure S2. Robust spectral estimation with finite-difference DPSS. **a**, **b** show different order DPSWF filters used for the spectrum reconstructions in panel **c** and **d**. The DPSS orders are in increasing order from $k = 0$ to $k = 5$. The sum of the filters (panel **b**) forms an approximate bandpass filter. **c** shows multiple single-taper reconstructions using the $k = 0$ filters only whose centre frequencies are shifted by $+i \times 0.5$ kHz with respect to the first set of filters for $i \in \{0, 1, 2, 3\}$. This results in different reconstructions. **d** shows a multitaper reconstruction using the same filter centre frequencies. The inset shows the sum of DPSWF filters used for each reconstruction.

The mean of the posterior, which serves as our final spectral estimate, and the posterior covariance are given by

$$\begin{aligned}\hat{\vec{S}} &= (\mathbf{F}^f T \Sigma_f^{-1} \mathbf{F}^f + \Sigma_0^{-1})^{-1} (\mathbf{F}^f T \Sigma_f^{-1} \vec{S}_y^f + \Sigma_0^{-1} \vec{S}_0), \\ \Sigma &= (\mathbf{F}^f T \Sigma_f^{-1} \mathbf{F}^f + \Sigma_0^{-1})^{-1}.\end{aligned}$$

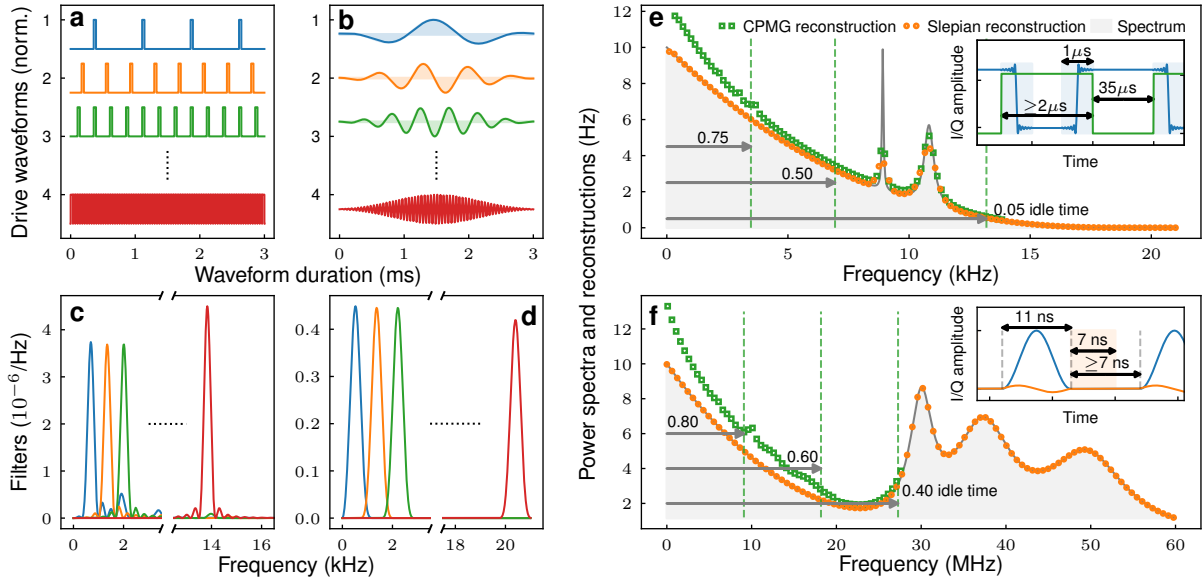
The posterior mean, plotted in Fig. 2(b) of the main text, demonstrates improved resolution of the narrowband features in the 8-12 kHz region of the spectrum.

A key difference between the experimental procedure and the proposal outlined in Ref. [23] is the use of $k = 0$ DPSS FFs versus multitaper FFs in the initial detection stage. What we term multitaper FFs are actually composite FFs formed by the summation of measurements taken with Slepian of different orders [22, 23]. Let $F_z^{(k)}(\omega, \tau)$ be the finite-difference FF in Eq. (17), corresponding to a Slepian of order k , and $\mathcal{S}_y^{(k)}(\tau)$ the resulting signal projection. For Slepians of orders $k = 0, \dots, K$, summing the signal projections weighted by coefficients c_k produces

$$\sum_{k=0}^K c_k \mathcal{S}_y^{(k)}(\tau) = \frac{1}{\pi} \int_0^\infty d\omega S_z(\omega) \left[\sum_{k=0}^K c_k F_z^{(k)}(\omega, \tau) \right],$$

where the quantity enclosed in the square brackets is the multitaper FF. With increasing K , the multitaper FF approaches an ideal bandpass filter, spectrally concentrated with uniform amplitude in its target band. In Fig. S2(c), the multitaper FF for $K = 5$, $\omega_s = 0$, and $c_0 = \dots = c_5 = 1$, is spectrally concentrated and nearly uniform within $(-2\pi W/\Delta t, 2\pi W/\Delta t)$. This uniformity is an asset for detection, since a narrowband spectral feature will produce nearly the same signal at any location within the target band. In contrast, the $k = 0$ Slepian FF is large in the center of the target band but falls to zero at the edges. As a result, a narrowband spectral feature near the edge of the band produces a substantially smaller signal projection than one near the center. The ability of $k = 0$ Slepian FFs to detect narrowband spectral features, consequently, is highly dependent on the positions of the filters in general. In Fig. S2(d), this is illustrated with eigenestimates produced by four sets of $k = 0$ Slepian FFs, each with slightly different positions along the frequency axis. The eigenestimates plotted in orange and green exhibit a large bump in the 8-12 kHz region since the second peak is positioned near the center of a band. The blue and red eigenestimates, on the other hand, register no bump since the second peak falls near the edge of a band. Thanks to their uniformity, multitaper FFs produce spectral estimates that are robust to position along the frequency axis. Figure S2(e), shows estimates produced by sets of multitaper FFs with the same positions and bandwidth as the $k = 0$ FFs. Unlike Fig. S2(d), each estimate exhibits a bump regardless of the FF positions.

Applying the multitaper estimation technique in experiments generally causes only a small overhead, as the number of measurements scale linearly with the number of included DPSS orders. However, experiments with engineered noise, as we have presented in the main text, require several random noise realizations to be implemented for each DPSS order (~ 400 in Fig. 2 in the main text) to ensure that the spectrum is sampled uniformly and thus get an accurate representation for all tapers. For this reason, the experiments reported in the main text only used single-taper estimation, based on the $k = 0$ DPSS order.



Supplementary Figure S3. Comparing CPMG and DPSS control for spectral estimation. **a, b** show the time-domain CPMG and DPSS waveforms respectively, both with a total duration of 3 ms. **c, d** show the corresponding FFs. **e** shows a numerically simulated spectrum reconstruction of a dephasing noise spectral density using both the CPMG and DPSS waveforms from panels a and b. The dashed lines indicate the maximum achievable frequency-cutoffs relating to different ratios of idle time vs. pulse time in the CPMG sequences. A value of e.g. 0.05 means that 95 % of the sequence consists of driven evolution. The inset shows a schematic *I/Q* waveform that closely resembles the actual CPMG waveforms we use in experiments. The shaded area highlights the ringing response of the *I/Q* baseband which we suppress using microwave blanking markers. **f** shows a reconstruction with different pulse parameters, inspired by a superconducting qubit device (see text). Here the π time and required buffer time are much shorter, which substantially increases the reconstruction range. The inset here shows again a sample *I/Q* waveform as used in the experiment.

Supplementary Note 5: Comparison to CPMG

Our DPSS control compares favorably to established pulse sequences for noise spectroscopy such as the CPMG sequence we consider in the main text [3, 13]. Here, we present a more detailed comparison of their spectral reconstruction capabilities performance in realistic settings, see Fig. S3. Specifically, we consider CPMG- and DPSS-based reconstructions under realistic experimental parameters taken from two distinct platforms: the ion trap from this publication (see Supplementary Note 3), and the superconducting qubit device from Ref. [33]. The key advantages that DPSS protocols afford manifest in terms of:

1. Reduced spectral leakage;
2. Ability to reconstruct (multiplicative) amplitude noise in addition to dephasing noise;
3. Increased scan range and spectral resolution through arbitrary waveform control.

The first two points arise directly from the nature of the DPSS waveforms as we outlined above and in the main text, while the last point illustrates a very common experimental subtlety, as we elucidate next.

To understand the advantages that DPSS control offers in terms of scan range, it is useful to re-examine the theoretical limitations of CPMG (see also [36] for an expanded discussion, applicable to more general pulsed protocols employing different sequences). A typical CPMG sequence of duration τ consists of n π -pulses separated by a n -dependent inter-pulse spacing, say, $\Delta\tau_n$, as depicted in Fig. S3 a) for rectangular pulses and varying n . Let τ_π denote the π -time, that is, the time required to apply a π -pulse. In the case where the pulses are (nearly) instantaneous, meaning that $\Delta\tau_n \approx \tau/n \gg \tau_\pi$, it is well known that the peak of the corresponding frequency domain filter occurs at $\omega \approx \pi/\Delta\tau_n$. Since CPMG spectroscopy enables the spectrum to be estimated at the location of this peak, the scan range in the (nearly) instantaneous-pulse regime is dictated by the minimum inter-pulse spacing, that is, $\omega_{\max} = \pi/\Delta\tau_{n_{\max}}$, where $\Delta\tau_{n_{\max}} \equiv \Delta\tau_{\min} > 0$ is the minimum possible inter-pulse spacing. Increasing the number of π -pulses in a fixed duration τ reduces $\Delta\tau_n$ and thus increases the scan range.

In practice, the finite duration of the control pulses, τ_π , may be non-negligible compared to $\Delta\tau_n$. In order to find the true maximum scan range, therefore, we need to take this into account. For CPMG, the FF of interest is

$$F_{zz}(\omega, \tau) \equiv \int_0^\tau ds e^{i\omega s} \cos \Theta(s), \quad (24)$$

which enters the qubit dynamics through the quantity

$$\langle |a_z^{(1)}(\tau)|^2 \rangle = \left\langle \left| \int_0^\tau ds \cos \Theta(s) \beta_z(s) \right|^2 \right\rangle = \frac{1}{\pi} \int_0^\infty d\omega |F_{zz}(\omega, \tau)|^2 S_z(\omega). \quad (25)$$

The integrand of Eq. (24) can be expressed as $\cos \Theta(t) \equiv y(t)H(\tau - t)$, where $H(t)$ is the Heaviside step function and $y(t)$ is a control-dependent function that is periodic in $2\tau/n$. For $k = 0, 1, 2, \dots$ and assuming rectangular π -pulses,

$$y(t) = \begin{cases} 1 & t \in [2k\tau/n, 2k\tau/n + \Delta\tau_n/2), \\ \cos[\Omega_\pi(t - 2k\tau/n - \Delta\tau_n/2)] & t \in [2k\tau/n + \Delta\tau_n/2, 2k\tau/n + \Delta\tau_n/2 + \tau_\pi), \\ -1 & t \in [2k\tau/n + \Delta\tau_n/2 + \tau_\pi, 2k\tau/n + 3\Delta\tau_n/2 + \tau_\pi), \\ -\cos[\Omega_\pi(t - 2k\tau/n - 3\Delta\tau_n/2 - \tau_\pi)] & t \in [2k\tau/n + 3\Delta\tau_n/2 + \tau_\pi, 2k\tau/n + 3\Delta\tau_n/2 + 2\tau_\pi) \\ 1 & t \in [2k\tau/n + 3\Delta\tau_n/2 + 2\tau_\pi, 2(k+1)\tau/n), \end{cases}$$

where $\Omega_\pi = \pi/\tau_\pi$. Note that in the limit of instantaneous π -pulses, $\tau_\pi \rightarrow 0$, $y(t)$ becomes a “flat-top” waveform. When τ_π is non-zero, we can write the CPMG FF in terms of Fourier coefficients, $a_\nu \equiv \frac{n}{\tau} \int_0^{2\tau/n} ds y(s) \cos(\pi n \nu s / \tau)$, that depend on $y(t)$. Explicitly, we have [37],

$$|F_{zz}(\omega, \tau)|^2 = \left| \pi \tau \sum_{\nu=1}^{\infty} a_\nu \left[e^{-i(\omega - \pi n \nu / \tau)} \text{sinc}\left(\frac{\omega \tau - \pi n \nu}{4\pi}\right) + e^{-i(\omega + \pi n \nu / \tau)} \text{sinc}\left(\frac{\omega \tau + \pi n \nu}{4\pi}\right) \right] \right|^2.$$

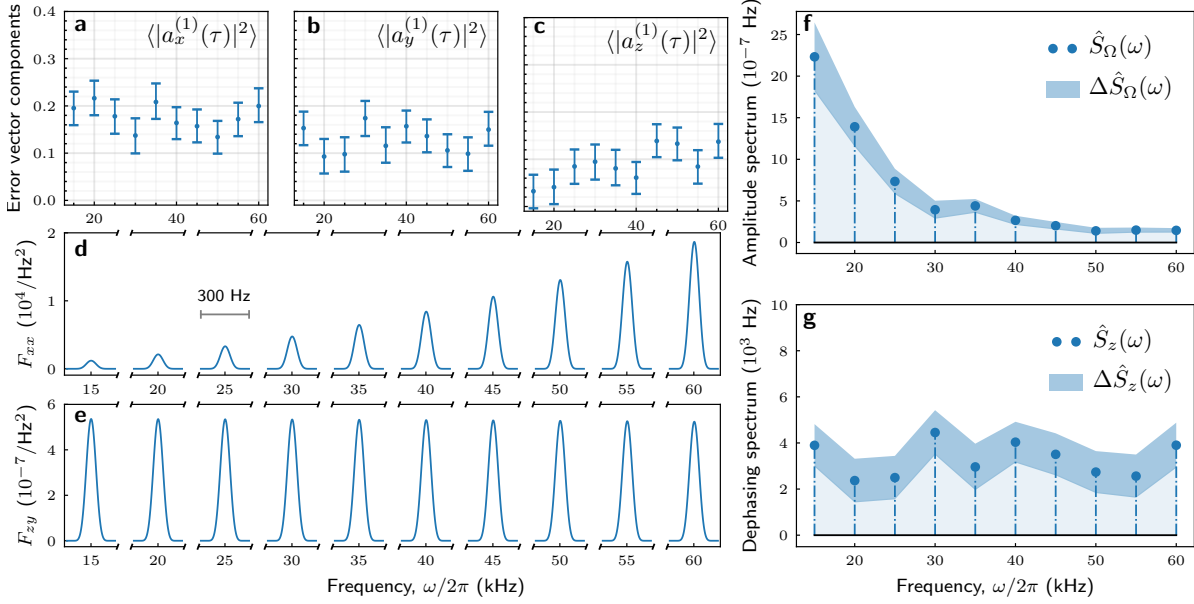
This FF consists of a series of peaks centered at integer multiples of $\omega = \pi n \nu / \tau$ with magnitudes dictated by the corresponding Fourier coefficients a_ν . The largest Fourier coefficient is a_1 , corresponding to the projection of $y(t)$ onto $\cos(\pi n t / \tau)$, which is also periodic in $2\tau/n$. Consequently, $|F_{zz}(\omega, \tau)|^2$ has a maximum peak centered at $\omega = n\pi/\tau$. The largest possible scan range is, thus, $\omega_{\max} = n_{\max}\pi/\tau$, where n_{\max} is the largest number of π -pulses that can be applied in a duration τ . In the limit of instantaneous pulses, the scan range reduces to the familiar expression $\omega_{\max} = \pi/\Delta\tau_{n_{\max}}$ we quoted above.

Realistic experimental settings face restrictions regarding the maximum number of pulses, n_{\max} , due to physical restraints on the achievable $\Delta\tau_{\min}$. The latter may arise, for instance, from transients in the drive response, as our chosen examples illustrate. Figure S3 e) and f) show two numerically simulated spectral reconstructions using both CPMG and DPSS waveforms under the ion-trap and the superconducting-qubit platforms, respectively. In both examples, we see that the leakage properties of the CPMG FFs manifests themselves as a significant overestimation of the actual noise strength at lower frequencies. Furthermore, the maximum reconstruction frequency for CPMG is limited due to features intrinsic to the implementation of the pulses.

In the case of the ion trap (panel e), $\tau_\pi \approx 35 \mu\text{s}$ and pulses are implemented using rectangular I/Q waveform shapes. However, to suppress the ringing response of the I/Q modulator to sharp waveform edges, additional blanking samples must be added to the waveforms, which effectively adds buffer time on either side of the pulse. In our setup, we require at least 10 samples which, with a typical sampling rate of $\omega_{\text{SR}}/2\pi = 10 \text{ MHz}$, restricts the interpulse spacing to be $\Delta\tau_n \geq 2 \mu\text{s} = \Delta\tau_{\min}$. If we impose a fixed sequence length, as we did for the exemplary $\tau = 3 \text{ ms}$ sequences in panels a) and b), the maximum integer number of pulses is given by $n_{\max} = N_{\text{tot}}/(N_\pi + N_{\text{blank}})$, where N_{tot} is the total number of samples in the waveform, N_{blank} is the number of blanking samples and N_π is the number of samples required for a π -pulse. For $\omega_{\text{SR}}/2\pi = 10 \text{ MHz}$, $N_{\text{tot}} = 30000$, $N_\pi = 350$, and with $N_{\text{blank}} = 10$, the maximum number of pulses that fit into our 3 ms sequence is $n_{\max} = 83$, which results in $\omega_{\max}/2\pi \approx 13 \text{ kHz}$. The scan range of DPSS controls, on the other hand, is set by the Nyquist frequency depending on the sampling rate, $\omega_{\max}/2\pi = \omega_{\text{SR}}/4\pi = 5 \text{ MHz}$. This is independent of the sequence duration τ .

For the superconducting qubit device considered in panel f), a minimum buffer time of $\Delta\tau_n = 7 \text{ ns}$ is required to ensure full separation between consecutive π -pulses [33]. Treating the pulses as instantaneous gives a maximum reconstruction frequency for CPMG of $\omega_{\max}/2\pi \approx 27.7 \text{ MHz}$, while the maximum reconstruction frequency for DPSS under a realistic sampling rate of e.g. $\omega_{\text{SR}}/2\pi = 1 \text{ GHz}$, would be $\omega_{\max}/2\pi = 500 \text{ MHz}$.

Lastly, comb-based spectral reconstruction protocols generally require the pulses to be narrow, so that the total pulse time remains short compared to the overall sequence length [2]. This can be quantified through the ratio between free evolution, or *idle* time, and driving time via $r_{\text{idle}} \equiv 1 - nT_\pi/\tau$, where $r_{\text{idle}} \equiv 1$ if there were no pulses in the sequence, and $r_{\text{idle}} \equiv 0$ if the sequence contains no idle time at all. If such a relative measure is imposed, the maximum reconstruction frequency becomes $\omega_{\max} = n_{\max}\pi/\tau = \pi(1 - r_{\text{idle}})/T_\pi$. Figure S3 shows the maximum achievable frequencies for different percentages of free evolution time for both platforms.



Supplementary Figure S4. Intrinsic noise spectral estimation. **a, b, c** show the measured error vector components [cf. Eqs. (6), (7)] taken with 10 band-shifted DPSS finite-difference waveforms with a duration of 20 ms sampled at 1 MHz with maximum Rabi rate $\Omega_{\max} \sim 15$ kHz. Each DPSS waveform was repeated 500 times and the error bars represent the standard deviations of the measurement outcomes. The corresponding amplitude and dephasing FFs are shown in **d** and **e** respectively, each plotted over a range of 300 Hz. **f** shows the estimated amplitude spectrum at the reconstruction frequencies. The shaded area shows the estimated variance of the spectrum as calculated through propagation of the measurement errors. **g** shows the dephasing spectrum reconstruction.

Supplementary Note 6: Application to intrinsic system noise

We applied the multi-axis sensing protocol to probe the intrinsic noise in our system and to measure both native amplitude and dephasing noise over a range of 0 – 60 kHz with 20 ms long waveforms. The measurements, FFs and spectrum reconstructions are shown in Fig. S4. In our measurements we scaled the amplitudes of the DPSS waveforms quadratically with increasing band-shift frequency, such that the amplitude of the dephasing filters, which scales as $\propto 1/\omega^4$ [cf. Eq. (17)], remains constant under band-shifting. This comes at the cost of an unequal magnitude of the amplitude filters, which only scale as $\propto 1/\omega^2$ [cf. Eq. (18)], and thus their amplitude increases with increasing band-shift.

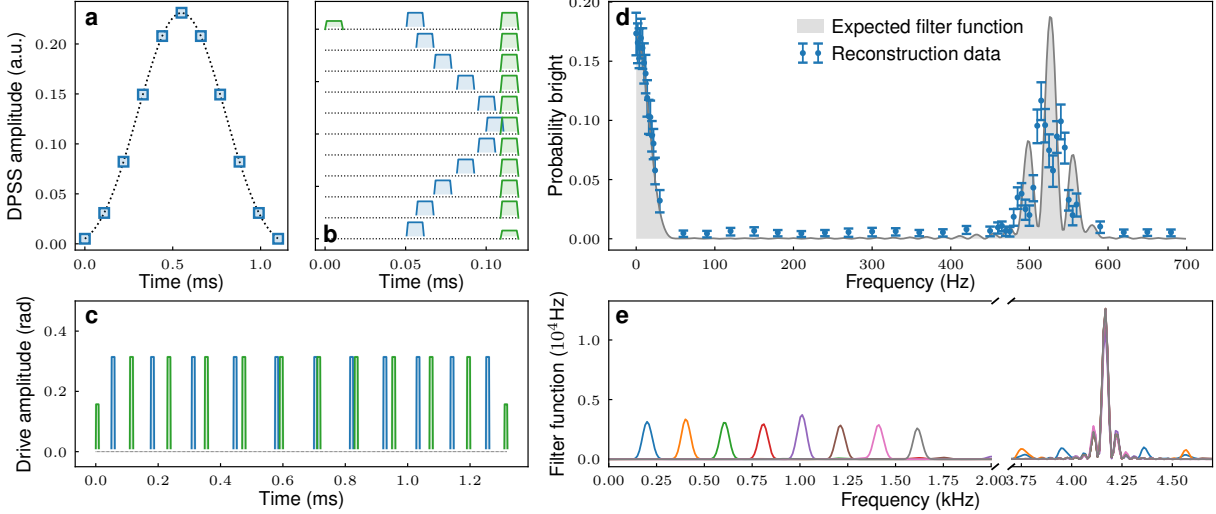
The error vector components that we measured are well above our measurement fidelity limit of about 0.003, however we observed no clear frequency-dependent signature that could be attributed to the underlying noise processes. In the reconstruction of the amplitude quadrature in Fig. S4(f), we observe a $1/\omega^2$ -type curvature which we believe may be an artifact of the scaling of the amplitude filters. We have separately performed a measurement (not shown) where the amplitude filters had their height held fixed, and we measured white noise at the 3×10^{-7} Hz level, which is consistent with the amplitude of last few reconstruction points in Fig. S4(f). Variations in measurement outcomes have thus far made it impossible to definitively identify whether the observed behavior is a faithful representation of the ambient noise process.

The estimated dephasing noise spectrum shown in Fig. S4(g) is white over the measured frequency range. The extracted amplitude, however, appears to be approximately two orders of magnitude larger than that extracted from a Ramsey measurement (via the DC noise component). T_2 echo measurements with CPMG waveforms yield similar results, which indicates that the DPSS dephasing filters may be sensitive to other noise processes in our experiment at such long interrogation times. For instance, we know that both intrinsic amplitude and dephasing noise are very low, and in fact our measured T_2 times are mostly limited by a reduction in ion fluorescence induced by ion-heating rather than pure dephasing noise.

In summary, reconstructing intrinsic amplitude and dephasing noise spectra remains an ongoing project on our particular experimental platform, and more careful investigations are needed to determine potential error sources other than the two noise processes considered in our present theoretical framework.

Supplementary Note 7: DPSS as discrete pulse sequences

For experimental platforms which do not allow for arbitrary waveform generation, it is still possible to leverage the spectral concentration properties of DPSS through pulse sequences (see Fig. S5). Consider a sequence of duration $\tau = N\Delta t$ consisting



Supplementary Figure S5. Discrete DPSS pulse sequences. **a** shows a sample DPSS which informs the pulse locations in the pulse sequence in panel **b**. The discrete points in time of the DPSS sequence in **a** are marked by the blue squares and correspond to the blue π -pulses in panel **b**. The green π -pulses mark the end of a segment in the sequence. The full, ravelled sequence is shown in **c** with the same colour coding. **d** shows an experimental FF reconstruction of a $k = 0$ DPSS pulse sequence with 25 segments with a π -time of $T_\pi = 35 \mu\text{s}$ and additional free evolution time of about 1.8 ms per segment, making the whole sequence 50 ms long. The FF of the corresponding sequence is mapped out by supplying a single-tone modulation to the FM input of the signal generator, and scanning the frequency of that modulation. **e** shows numerically calculated FFs of a series of bandshifted DPSS pulse sequences with 50 segments of 220 μs duration and with a π -time of $T_\pi = 10 \mu\text{s}$. The main harmonic at $1/(220 \mu\text{s} + 2 \times 10 \mu\text{s}) \approx 4.166 \text{ kHz}$ is the same for all filters.

of $2N - 1$ π -pulses about σ_x , applied at times t_1, \dots, t_{2N-1} . The FF $|F_{zz}(\omega, \tau)|^2$, which arises in $\langle |a_z^{(1)}(\tau)|^2 \rangle$ in Eq. (25), is spectrally concentrated about ω_s if the pulse times are chosen so that they depend on a COS modulated DPSS,

$$t_n = \begin{cases} n\Delta t/2, & n \text{ even}, \\ [c_\tau \cos(\frac{n-1}{2}\omega_s\Delta t)v_{\frac{n-1}{2}}^{(k)}(N, W) + n\Delta t]/2, & n \text{ odd}. \end{cases} \quad (26)$$

Here, c_τ is a scaling factor in units of time, satisfying $c_\tau v_n^{(k)}(N, W) < \Delta t$ for all n . A sample sequence generating a $k = 0$ DPSS FF centered at $\omega_s = 0$ is illustrated in Fig. S5 (a)-(c). Experimental reconstructions of such a FF centered at $\omega_s = 0$ is shown in S5 (d). The signal measured at $\sim 530 \text{ Hz}$ is the harmonic of the sequence generated by the periodic spacing of the π -pulses at the end of each segment (green pulses in Fig. S5(b)). If the target spectrum to be estimated has a very wide frequency range, care must be taken in ensuring that leakage bias resulting from that may be accounted for.

To better understand the spectral concentration properties of the FFs generated by these pulse sequences, consider the idealized case in which the π -pulses are instantaneous in time and the amplitude control waveform takes the form

$$\Omega(t) = \pi \sum_{n=1}^{2N-1} \delta(t - t_n).$$

For this amplitude waveform, $\cos \Theta(t) \mapsto y(t)$ in Eq. (25), where $y(t)$ is a switching function that toggles between ± 1 with every application of a π -pulse. More concretely, the switching function takes the values

$$y(t) = \begin{cases} 1 & 0 \leq t < t_1, \\ -1 & t_1 \leq t < t_2, \\ 1 & t_2 \leq t < t_3, \\ \vdots & \\ 1 & t_{2N-2} \leq t < t_{2N-1}, \\ -1 & t_{2N-1} \leq t < \tau. \end{cases}$$

The Fourier transform is then

$$F_{zz}(\omega, \tau) = \int_0^\tau ds e^{i\omega s} y(s) = \sum_{m=0}^{N-1} e^{i\omega m \Delta t} \int_0^{\Delta t} ds e^{i\omega s} y(s + m\Delta t).$$

If ω_c is the approximate cutoff frequency of the spectrum, i.e., $S_z(\omega) \approx 0$ for $\omega > \omega_c$, and $\omega_c \Delta t \ll 1$, then $e^{i\omega m \Delta t} \approx 1$ in the above expression. From Eq. (26), letting $n' = 2m$,

$$\int_0^{\Delta t} ds y(s + m\Delta t) = \int_{t_{n'}}^{t_{n'+1}} ds - \int_{t_{n'+1}}^{t_{n'+2}} ds = c_\tau \cos(m\omega_s \Delta t) v_m^{(k)}(N, W).$$

The FF entering Eq. (25) is then

$$|F_{zz}(\omega, \tau)|^2 \approx \left| \sum_{m=0}^{N-1} e^{i\omega m \Delta t} c_\tau \cos(m\omega_s \Delta t) v_m^{(k)}(N, W) \right|^2 \approx c_\tau^2 \left[|U^{(k)}(N, W; \omega - \omega_s)|^2 + |U^{(k)}(N, W; \omega + \omega_s)|^2 \right],$$

which is spectrally concentrated about ω_s , as desired.